Bolt Beranek and Newman Inc.

NASA CONTRACT NO. NAS2-9549
REPORT NO. 3563

ACOUSTICAL PROPERTIES OF MATERIALS AND MUFFLER CONFIGURATIONS FOR THE 80 x 120 FOOT WIND TUNNEL

25 AUGUST 1977

TERRY D. SCHARTON
MATTHEW D. SNEDDON

SUBMITTED TO:

NATIONAL AERONAUTICS AND SPACE ADMINISTRATION
AMES RESEARCH CENTER
MOFFETT FIELD, CALIFORNIA 94035

NASA Contract No. NAS2-9549
Report No. 3563

ACOUSTICAL PROPERTIES OF MATERIALS AND MUFFLER CONFIGURATIONS FOR THE 80 X 120 FOOT WIND TUNNEL

25 August 1977

Terry D. Scharton
Matthew D. Sneddon

Submitted to:

National Aeronautics and Space Administration
Ames Research Center
Moffett Field, California 94035

TABLE OF CONTENTS

LIST OF FIGURES

LIST OF FIGURES (Cont'd)

LIST OF TABLES

SUMMARY

Two muffler configurations have been developed on the basis of analyses, laboratory experimentation, and extensive NASA Ames Research Center wind tunnel tests. One configuration is a highly optimized fiberglass-filled design, and the other is a novel perforated plate no-fuzz design, similar to those used in aircraft engine inlets. The acoustic performances of both designs, and particularly, the perforated plate configuration, are strongly influenced by the impedance of the acoustic materials and by the configuration details of the built-up systems.

To support the design of these mufflers, techniques for measuring the impedance of the complete configurations and of porous plates with grazing flow are herein investigated and utilized, and changes in the configuration parameters to enhance acoustic performance are explored. The feasibility of a pulse reflection technique for measuring the impedance of built-up structures in situ is demonstrated, but the technique is currently not sufficiently accurate to provide quantitative design data. Therefore, a second technique involving the use of an open-end impedance tube with grazing flow is used to obtain detailed design data for the perforated plate configuration. Acoustic benefits associated with configuration changes such as curving the baffles, spacing and staggering baffle partitions, and techniques for alleviating baffle self-generated noise are described.

1.0 PULSE REFLECTION IMPEDANCE MEASUREMENT TECHNIQUE

Experiments were conducted to determine the applicability of a pulse reflection technique for measuring the impedance of materials and muffler configurations for the 80 x 120 foot wind tunnel. The technique utilizes an impulsive source, a microphone to measure the direct pulse from the source, a second microphone to measure the pulse reflected from the specimen, and a two-channel fast Fourier transform (FFT) analyzer to determine the magnitude and phase of the reflection coefficient--from which the impedance is readily calculated.

This technique offers the potential advantage that it may be used in situ with large built-up specimens where other impedance measurement techniques are not appropriate. Herein we describe the experiment design, characteristics of three candidate sources, and data obtained for a 4-inch layer of fiberglass and for an asphalt surface. The results obtained with this technique are in qualitative agreement with other available data, but we selected an alternative open-end impedance tube method discussed in Section 2.0 for quantification of the acoustical properties of candidate materials for the 80 x 120 foot wind tunnel.

1.1 Experiment Design

The test set up for the pulse reflection impedance measurement experiment is shown in Fig. 1. Two microphones and an impulsive sound source are mounted on a stand at heights of 181 inches, 87 inches, and 47 inches, respectively. The distances of the microphones and source above the reflecting ground plane are selected so that the reflected pulse arriving at Microphone B,

Path B Reflected		Path A Direct	
87 In.	(2210 mm)	181 In.	(4594 mm)
+47 In.	(1192 mm)	- 47 In.	(1192 mm)
134 In.	(3402 mm)	134 In.	(3402 mm)

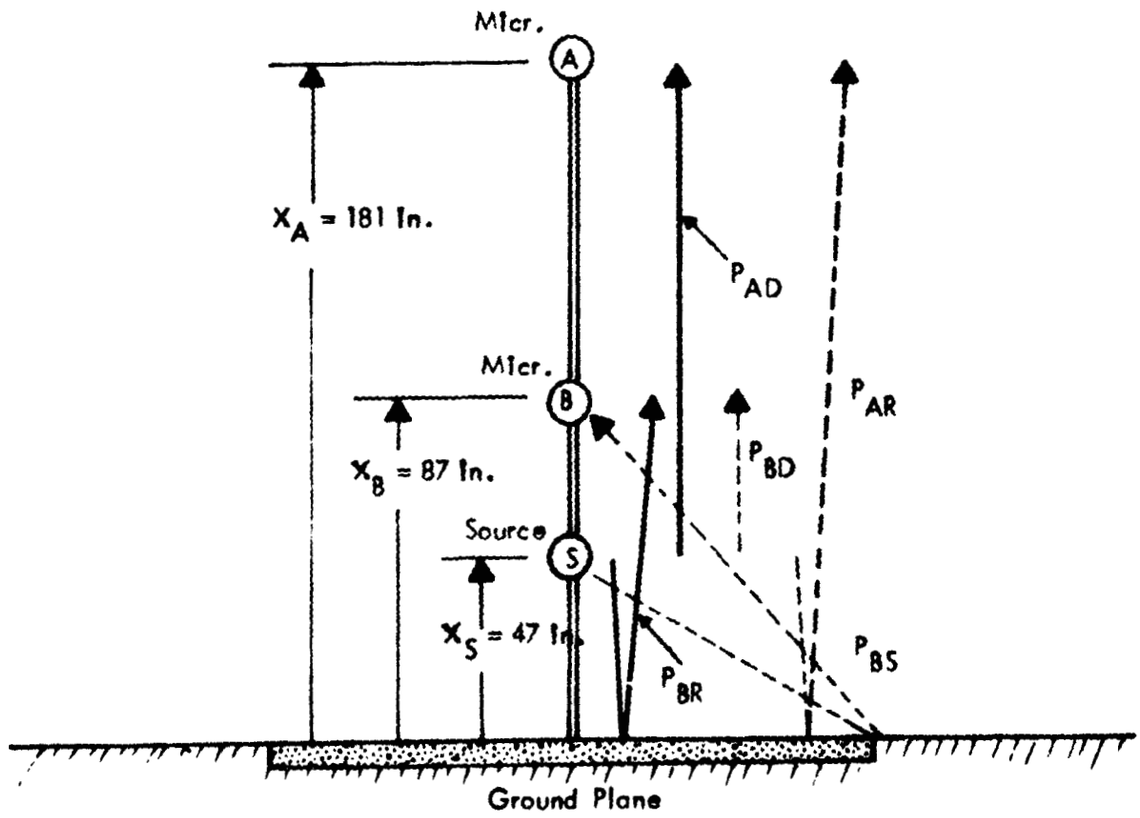

FIGURE 1. PULSE REFLECTION IMPEDANCE MEASUREMENT TEST SET-UP

which travels the path P_{BR}, arrives at the same instant as the direct pulse arrives at Microphone A, having traveled the path P_{AD}.

As indicated in Fig. 1 both Microphone A and B are also subjected to a number of unwanted pulses involving direct, reflected, or scattered paths. The design of the experiment involves the selection of the impulsive source and the source and microphone spacings so as to obtain maximum signal strength in the frequency range of interest, and to facilitate the deletion of the extraneous unwanted signals.

Typical time traces for Microphones A and B as captured by the two-channel FFT analyzer are illustrated in Fig. 2. For convenience, we will assume that the traces start when the impulsive source fires. However, in practice either the Microphone B or A signal is used to trigger the analyzer and the amount of data displayed before the trigger pulse is dependent on the specific FFT analyzer used. We used the Spectral Dynamics Model 360 which retains 1/10th of sample length prior to the triggering pulse.

The illustrated time history for Microphone B shows three captured signals: a direct pulse, a reflected pulse, and a scattered pulse. Since we desire that Channel B of the analyzer retain only the reflected pulse data in the middle of the trace, we must have the capability to delete the data outside the desired data window. The Spectral Dynamics Model 360 has a convenient joy-stick control for this editing. Other analyzers offer comparable means of setting data outside this window to zero.

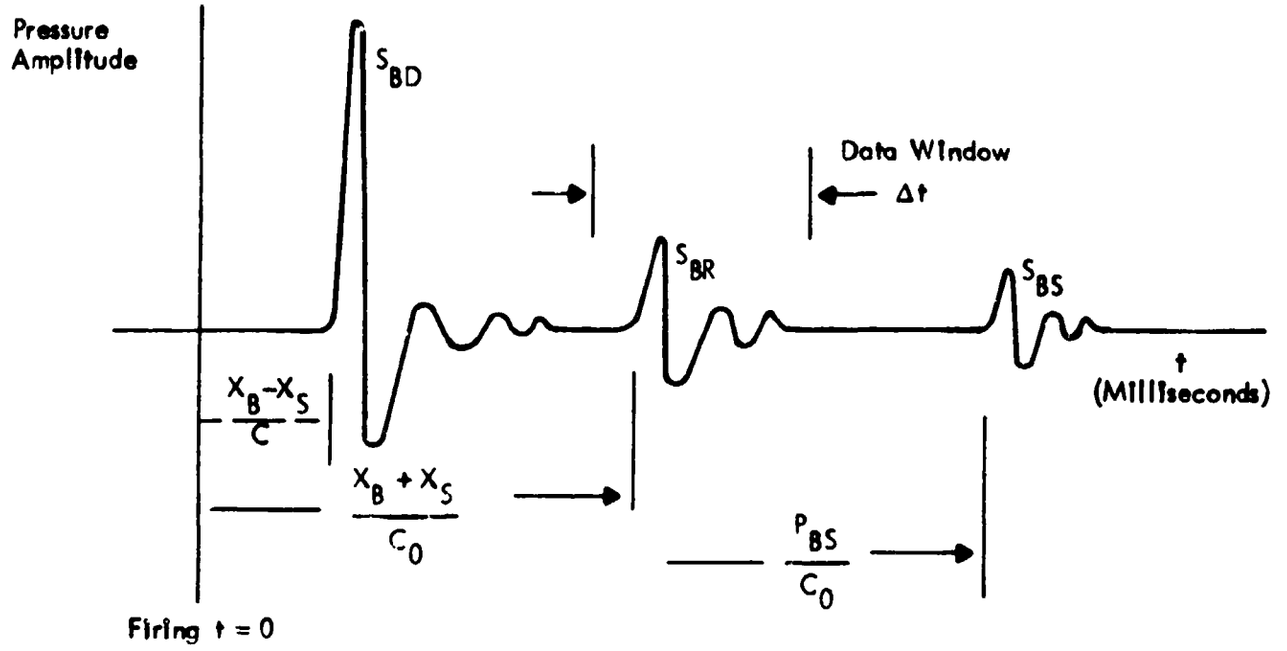

Microphone B - Time History

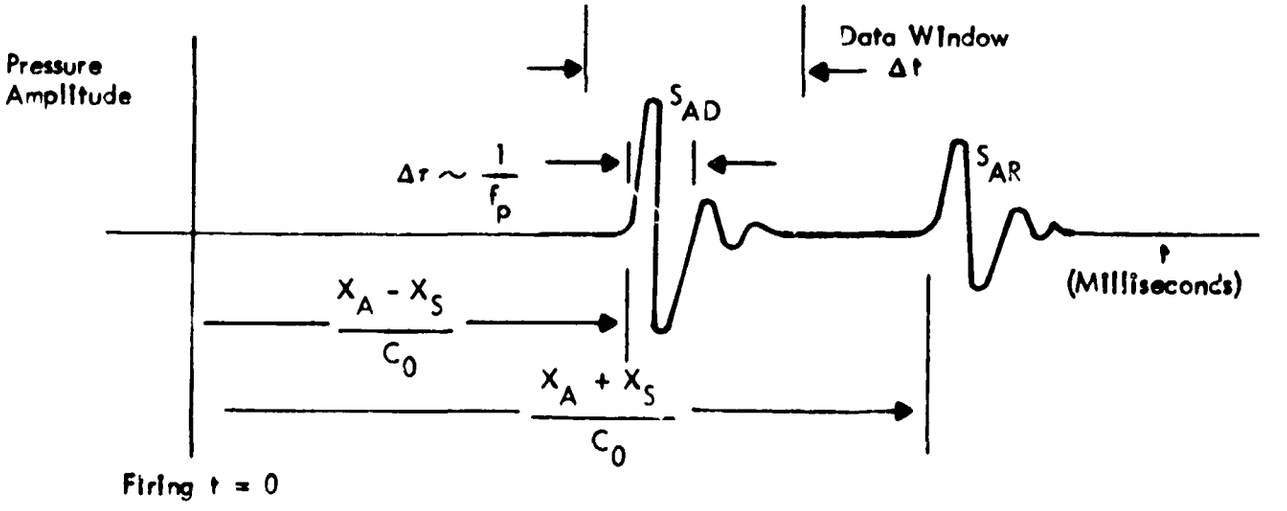

Microphone A - Time History

FIGURE 2. ILLUSTRATIVE PULSE TIME HISTORIES

Similarly, we desire to retain only the direct pulse data arriving at Microphone A which requires deletion of the reflection from the ground plane and any other reflections from nearby objects (not shown). With the reflected pulse stored in Channel B of the analyzer and the direct pulse stored simultaneously in Channel A, the analyzer can on command calculate and display the spectrum of each pulse and the magnitude and phase of the desired reflection coefficient.

Isolation of the desired direct and reflected signals involves a number of design considerations. First, the sound source must provide a pulse with sufficient amplitude and frequency content to yield good signal to noise in the frequency range of interest. In general terms, the low frequency limit of the data is inversely proportional to the width of the pulse, and the high frequency limit to the rise time of the pulse. We require data at frequencies below 1000 Hz, thus we need a pulse width greater than one millisecond.

Referring to the time history for Microphone B and Fig. 1, the time between the direct and reflected pulse arrival at Microphone B is equal to twice the source height divided by the speed of sound. The source height of approximately 47 inches was chosen to enable deletion of the direct pulse from the Microphone B signal. The distance of Microphone B above the source is limited by the strength of the direct pulse that can be tolerated at Microphone B without overloading the microphone and amplifiers so that Channel B can properly record the subsequent desired reflected pulse. In our case, Microphone B was located 40 inches above the source, and this proved just marginal. In many cases Microphone B did overload, and we had to reject data from that experiment. Once the height of the source and Micro-

phone B are selected, the interval between the reflected pulse and the scattered pulse at Microphone B depends only on the width of the impedance specimen. It is necessary to have a large enough sample so that reflections from the discontinuities at the edge of the sample do not compromise the reflected pulse at Microphone B. In the fiberglass experiment a sample width of 16 inches was used to separate the reflected and scattered pulse arrival times at Microphone B by approximately 8 milliseconds. Once the height of the source and Microphone B have been determined, the height of Microphone A is determined by the requirement that the direct signal arrives simultaneously with the reflected signal at Microphone B, i.e., $x_A = x_B + 2x_S$. With the source and microphones so arranged, the time between the direct and reflected signals at Microphone A will be identical to that for Microphone B, and therefore acceptable.

As our test set-up illustrates, application of this technique at relatively low frequencies requires relatively large source and microphone spacings which can cause a number of problems. First, one must take care that other reflecting surfaces are far enough removed so as not to interfere with the data. Second, in order to maintain the proper phase relationships between the direct and reflected pulse, the source must be compact and the height of the source and microphones must be known accurately within a small fraction of the acoustic wave length. The uncertainty in phase angle $\Delta\phi$ due to an uncertainty in the path difference Δx for the reflected wave at Microphone B and the direct wave at Microphone A is

$$\Delta\phi = 360^\circ \frac{\Delta x}{\lambda} \qquad (1)$$

where λ is acoustic wave length. In our case, for an estimated uncertainty in path length of ±10 millimeters, we anticipate an uncertainty in phase angle of ±1° at 100 Hz, ±10° at 1000 Hz, and ±30° at 3000 Hz.

A number of variations on the set-up used here are possible. One variation involves locating Microphone B below the source. In this case, referring to Fig. 2, the time interval between the direct and reflected pulse at Microphone B is decreased to $2x_B/c_0$, which can make rejection of the direct pulse more difficult. Another variation which has been used successfully to measure the absorption coefficient involves using a steady-state broadband noise source, for example, a loudspeaker. This technique bears investigation for impedance measurement; however, problems may arise if the speaker is not compact, i.e., if it is small compared to an acoustic wavelength at the measurement frequencies of interest.

Some judgement is required in editing to construct the data window at. Too small a window reduces the low frequency signal and also generates spurious high frequency noise associated with the convolution of the step function window with the pulse tail. Selection of the window width should be guided by theoretical considerations, such as those set forth in Reference 1, and by trial and error to determine that the final result is not sensitive to small variations in the window width.

1.2 Candidate Impulsive Sources

The time histories and spectra of several sources including a spark discharge, a starter pistol, and a red balloon were measured using the instrumentation shown in Fig. 3. Figure 4 shows the time history and the spectra for two repeated firings

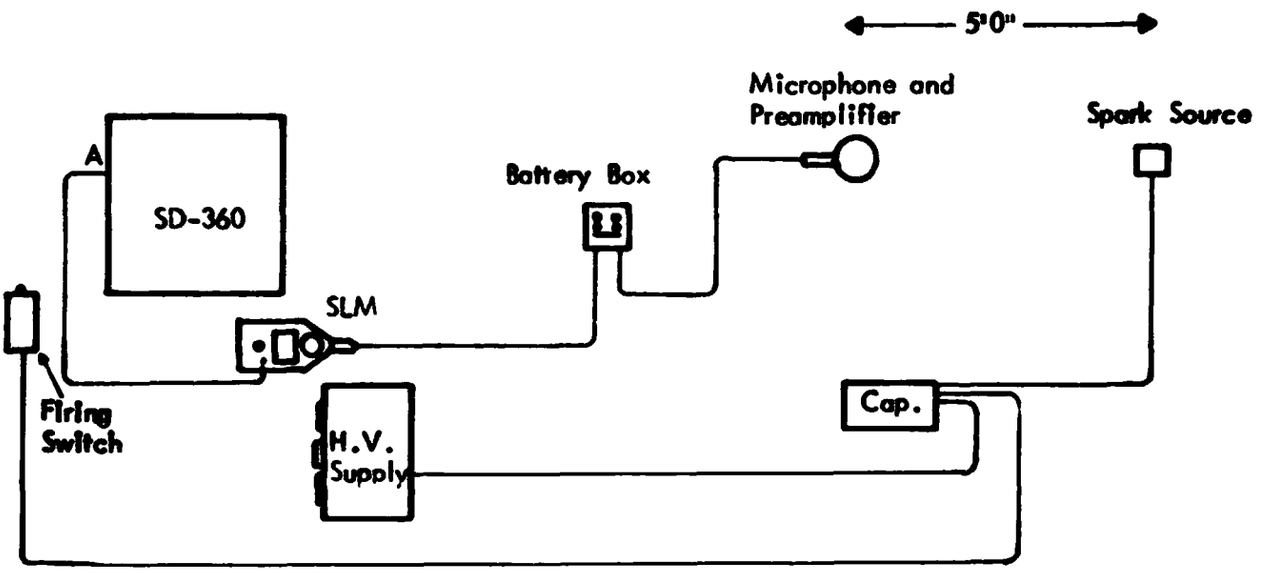

Sound Level Meter: B & K Type 2203

Preamplifier: GR P42

Microphone: B & K Type 4133

Spark Supply Voltage: 2700 VDC

The Measurement Angles are Defined as Follows:

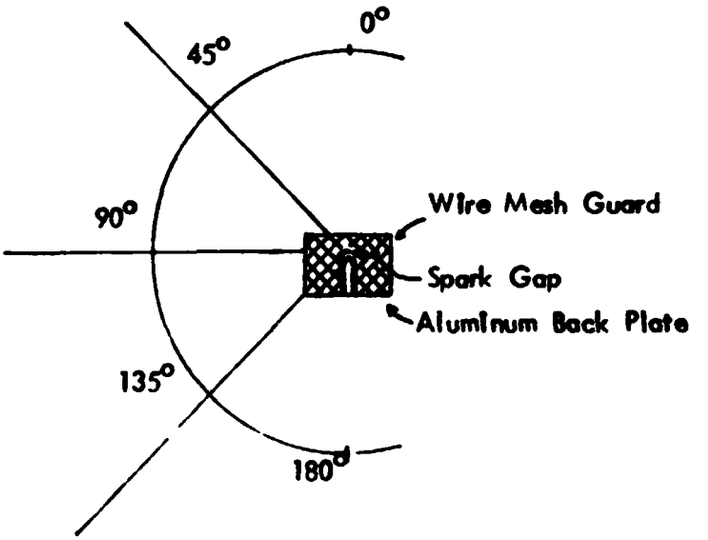

FIGURE 3. SPARK SOURCE MEASUREMENT SET-UP

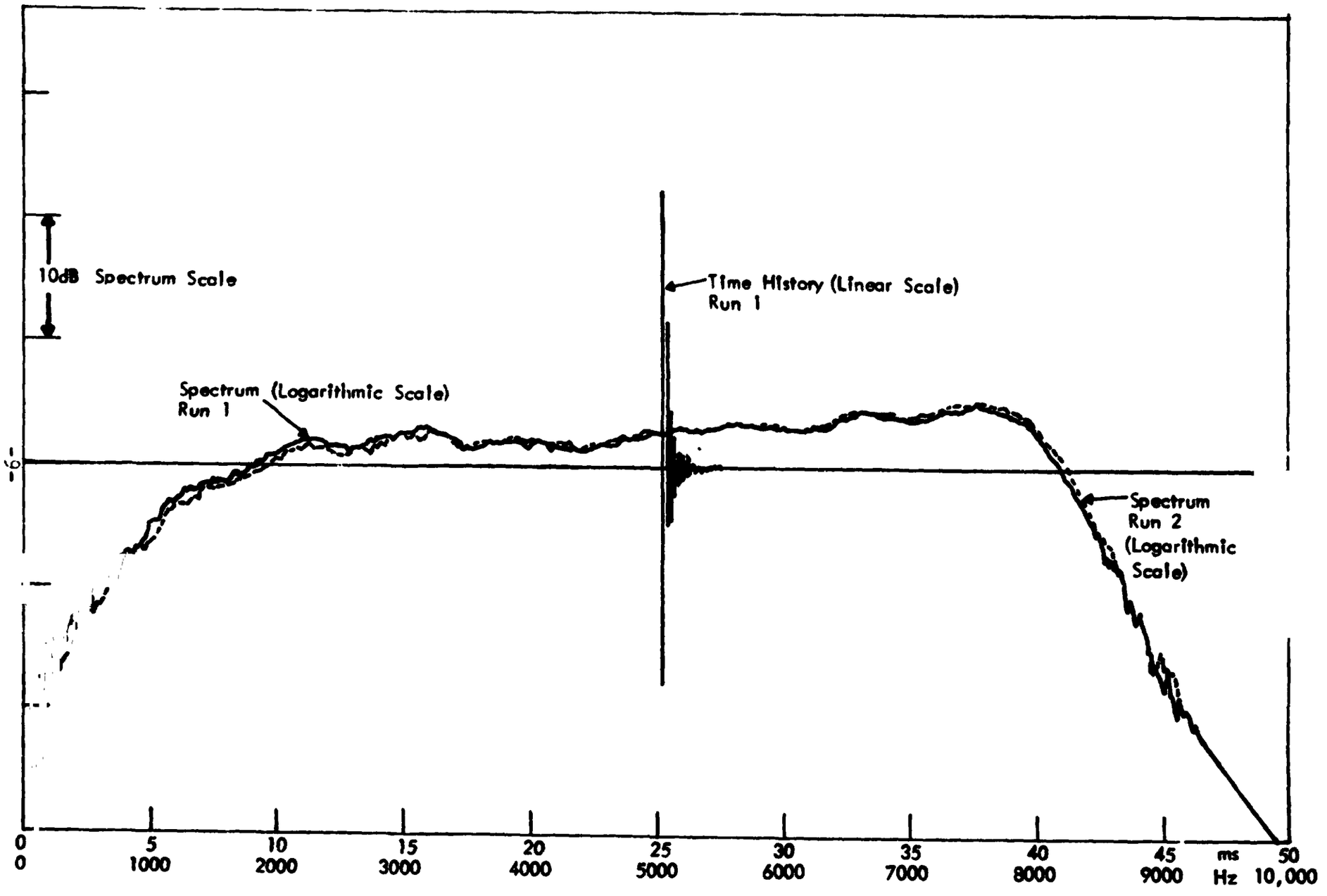

FIGURE 4. SPARK SOURCE 90° TIME HISTORY (0 - 50 ms) AND REPEAT SPECTRA (0 - 10 KHz)

of the spark source with the microphone located 5 feet to the side of the source as illustrated in Fig. 3. The spectra of the two firings shown in Fig. 4, and many other firings conducted during this series of tests, indicate that the spark source is extremely repeatable, which is an advantage if one desires to average together the results of many experiments in order to minimize errors in digital computation and editing. The roll-off in the spectra shown in Fig. 4 at 8000 Hz is due to the anti-aliasing filter and not to the spectral energy content as shown by the extended frequency spectrum in Fig. 5. The spark pulse width is approximately 0.15 milliseconds, and the peak in the energy spectrum occurs at f = 1 ÷ .15 ms = 7000 Hz. The spectrum is 10 dB down at 1000 and 15,000 Hz and 20 dB down at 300 and 20,000 Hz. Thus the spark source has considerable energy in the high frequency regime but is somewhat weak in the frequency range below 1000 Hz, which is of interest in the 80 x 120 foot wind tunnel.

Figure 6 shows the directivity of the spark source over the frequency range from 0 to 10,000 Hz for the five measurement angles defined in Fig. 3. Some of the directivity effects shown in Fig. 6 are due to the reflective and scattering effects of the aluminum back plate and wire-mesh grid used to mount the spark unit.

Figure 7 shows for the starter pistol the time history from 0 to 50 milliseconds and the spectra from 0 to 10,000 Hz. For these measurements, the pistol was held in a horizontal position and the measurements were conducted 5 feet directly to the side of the chamber. The data shown in Fig. 7 indicates that the starter pistol is not as repeatable from shot to shot as the spark source, but the starter pistol has considerably more low frequency

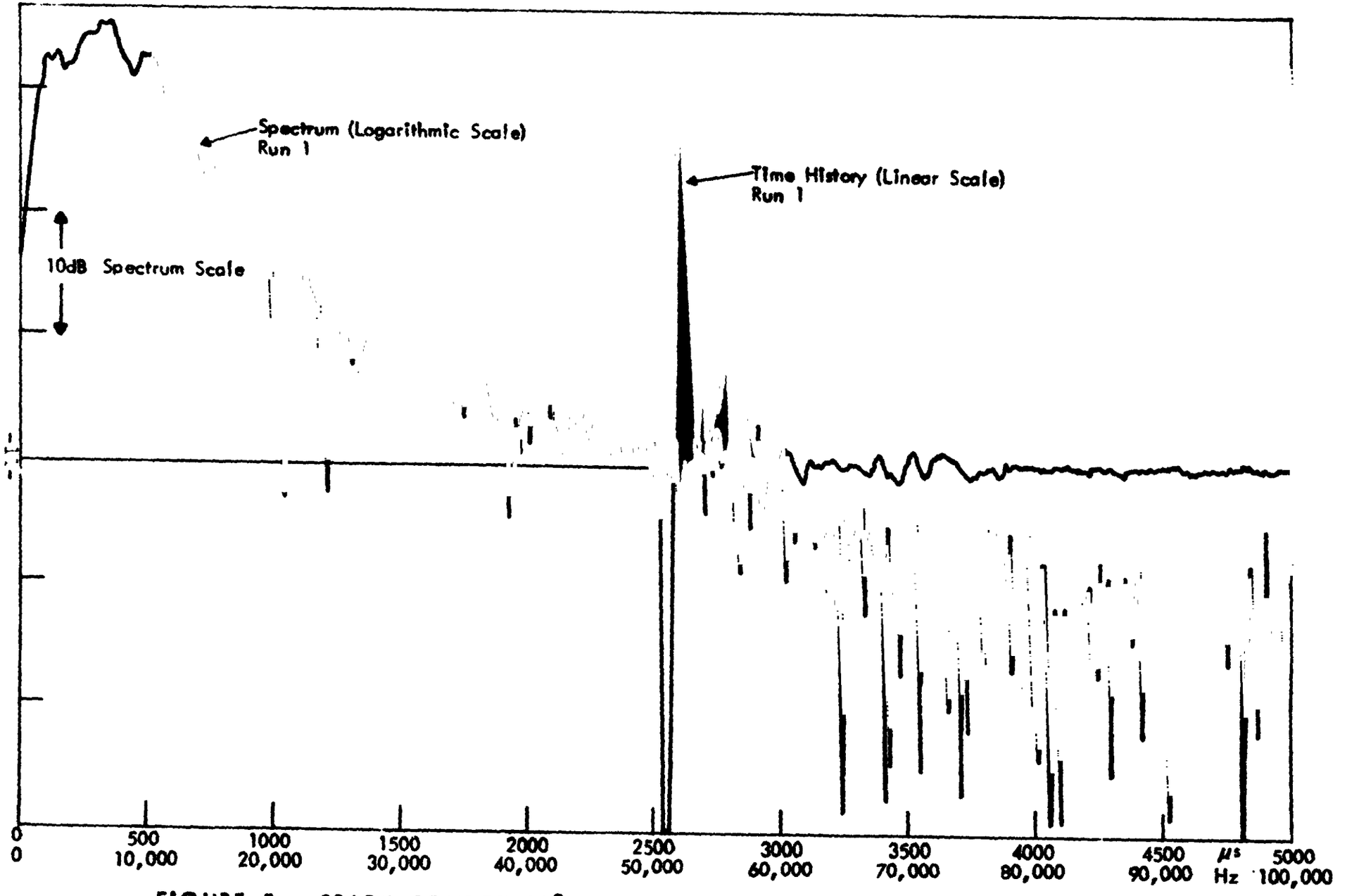

FIGURE 5. SPARK SOURCE 90° TIME HISTORY (0 - 5000 μs) AND SPECTRUM (0 - 100 KHz)

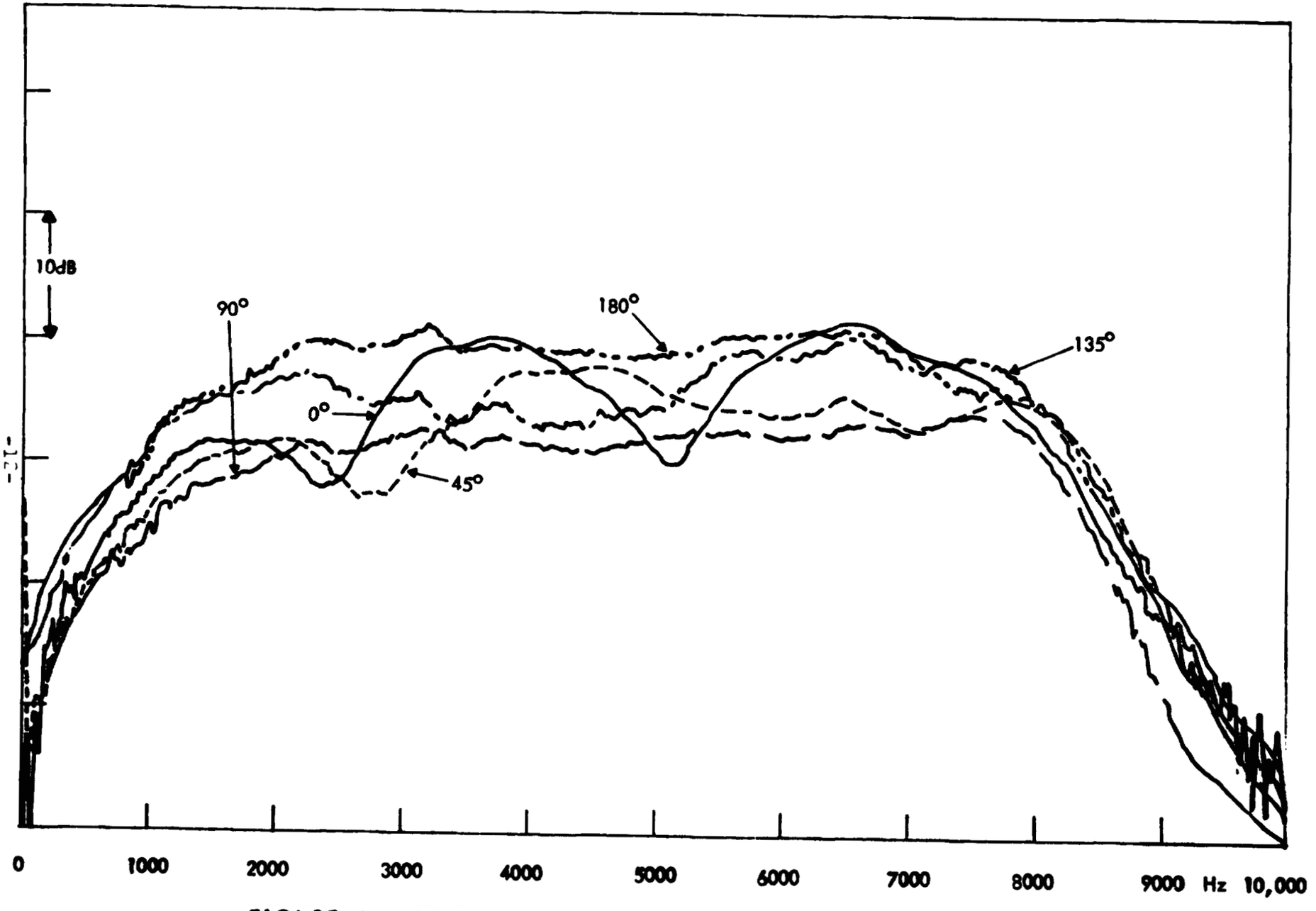

FIGURE 6. SPARK SOURCE SPECTRA (0 - 10 KHz) DIRECTIVITY

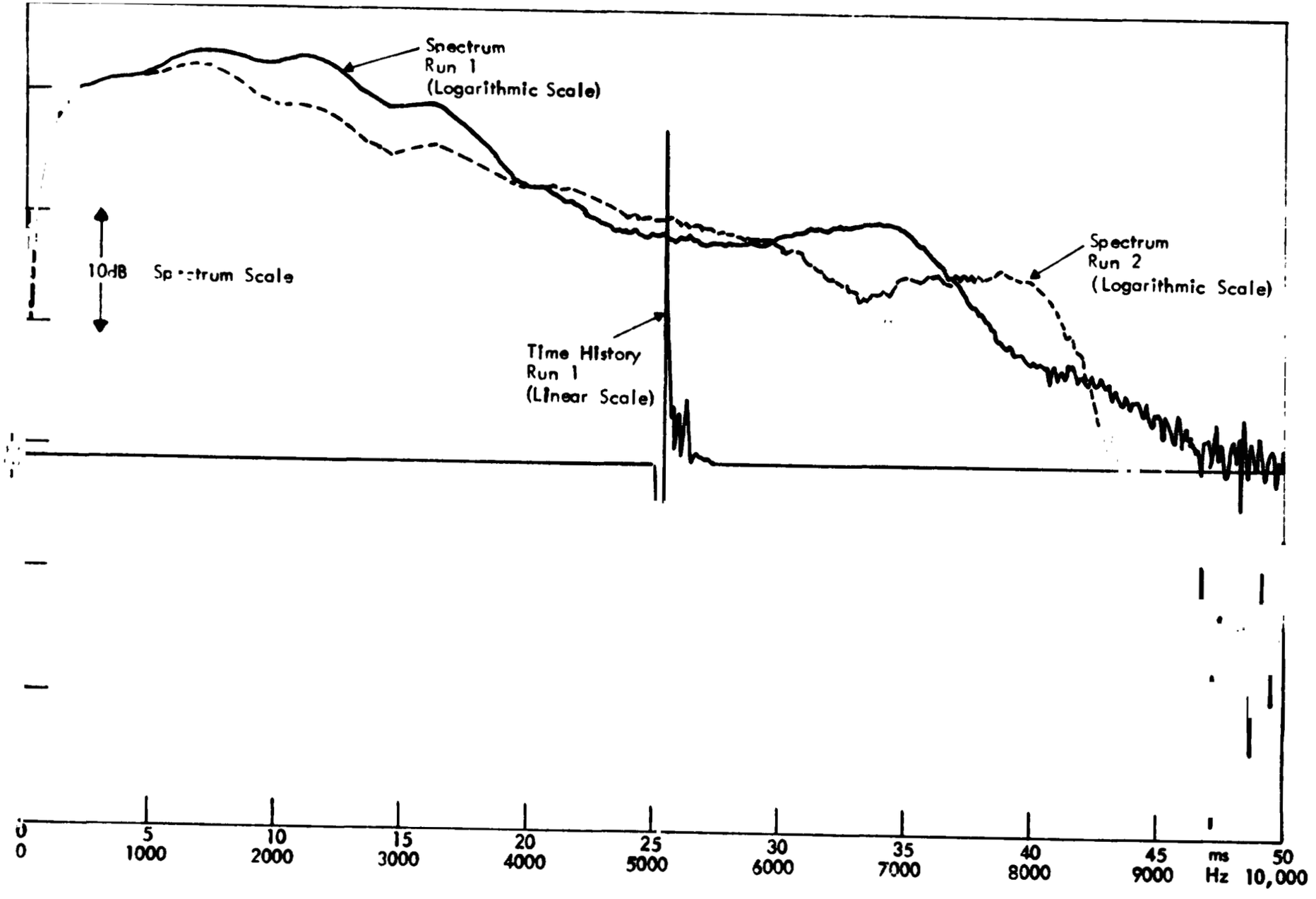

FIGURE 7. STARTERS PISTOL 90° (ABREAST) TIME HISTORY (0 - 50 ms) AND REPEAT SPECTRA (0 - 10 KHz)

energy. The starter pistol pulse duration is approximately 0.8 milliseconds, and the spectrum peaks at approximately 1200 Hz. The spectrum is 10 dB down at 100 and 4000 Hz and 20 dB down at 50 and 7500 Hz.

Figure 8 shows the time history and two repeated spectra for a red balloon approximately 6 inches in diameter. The primary pulse width is approximately 2 milliseconds, and the spectrum peaks at approximately 400 Hz. The pulse and spectrum levels vary widely from pop to pop with the red balloon.

The starter pistol was selected for these experiments because it represented the best compromise between the spark source and the red balloon. The spark source had insufficient energy at the low frequencies, and the red balloon pulse continued to ring for such a long period that it was not possible to edit out the primary pulse from the unwanted microphone signals. The barrel of the pistol was held horizontal, but the grip was rotated 90° to the side so that the directivity was nominally equal in the upward and downward directions. A long string, tied to the trigger, was used to fire the pistol.

1.3 Impedance Measurements

Raw data obtained using the technique to measure the impedance of a 4-inch layer of Type 701 Fiberglas placed on top of a large asphalt surface is contained in Figs. 9, 10, and 11. Figure 9 shows the edited reflected pulse measured with Microphone B and stored in Channel B of the analyzer, and the direct pulse measured with Microphone A and recorded in Channel A of the analyzer. Figure 10 shows the corresponding computed spectra of the pulses.

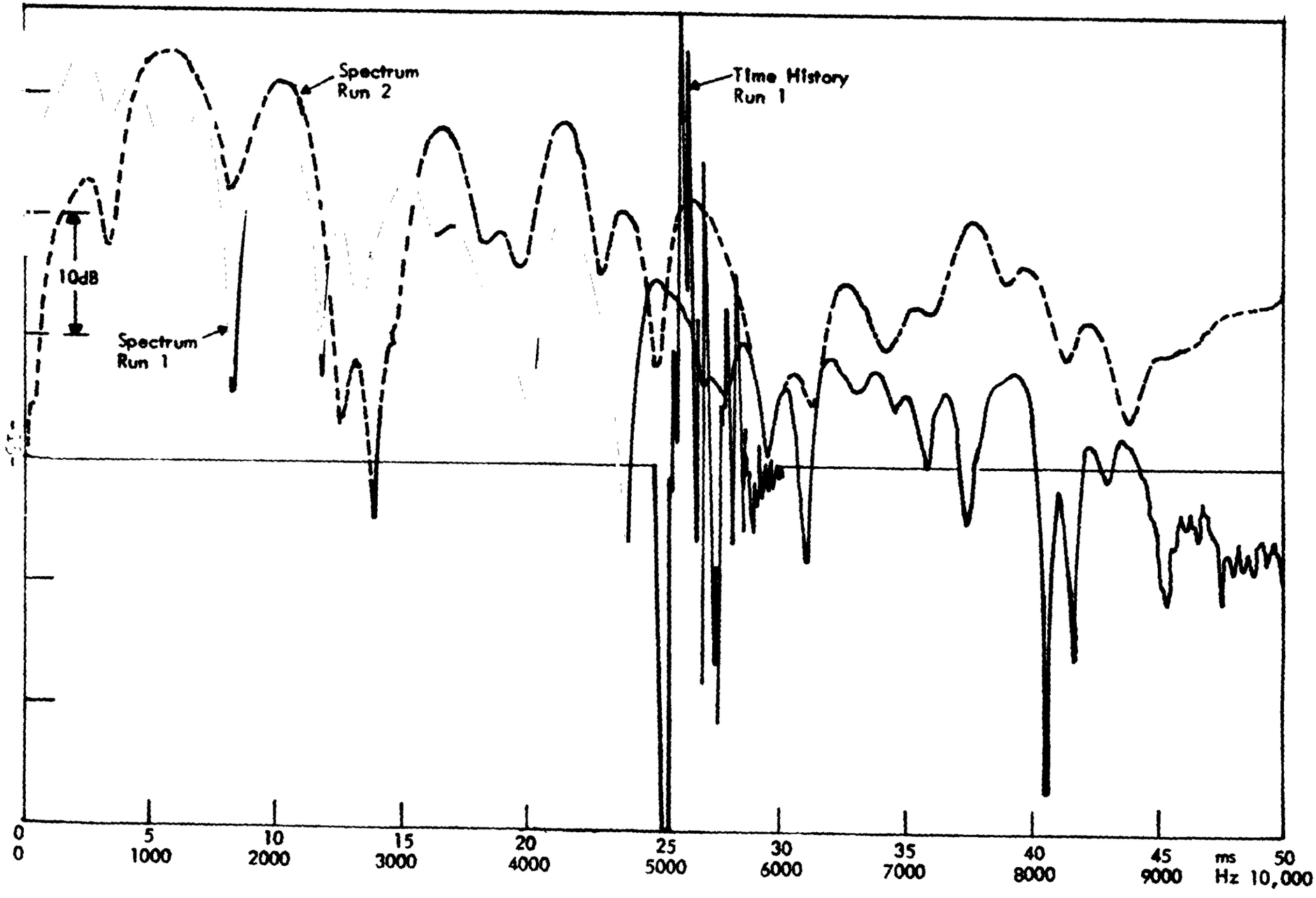

FIGURE 8. RED BALLOON TIME HISTORY (0 - 50 ms) AND REPEAT SPECTRA (0 - 10,000 Hz)

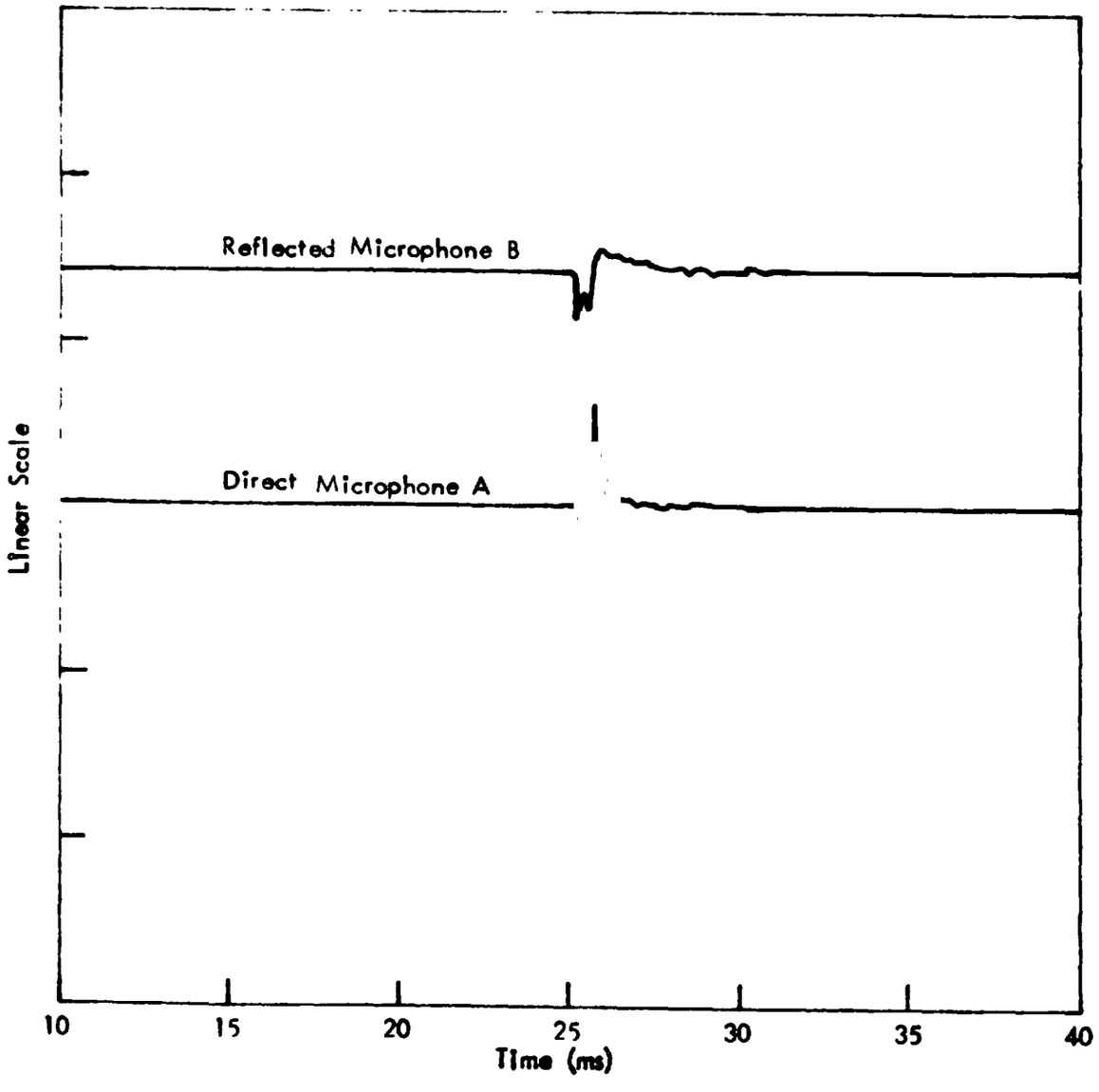

FIGURE 9. EDITED TIME HISTORIES OF REFLECTED AND DIRECT PULSES FROM 4" LAYER OF TYPE 701 FIBERGLAS ON TOP OF ASPHALT

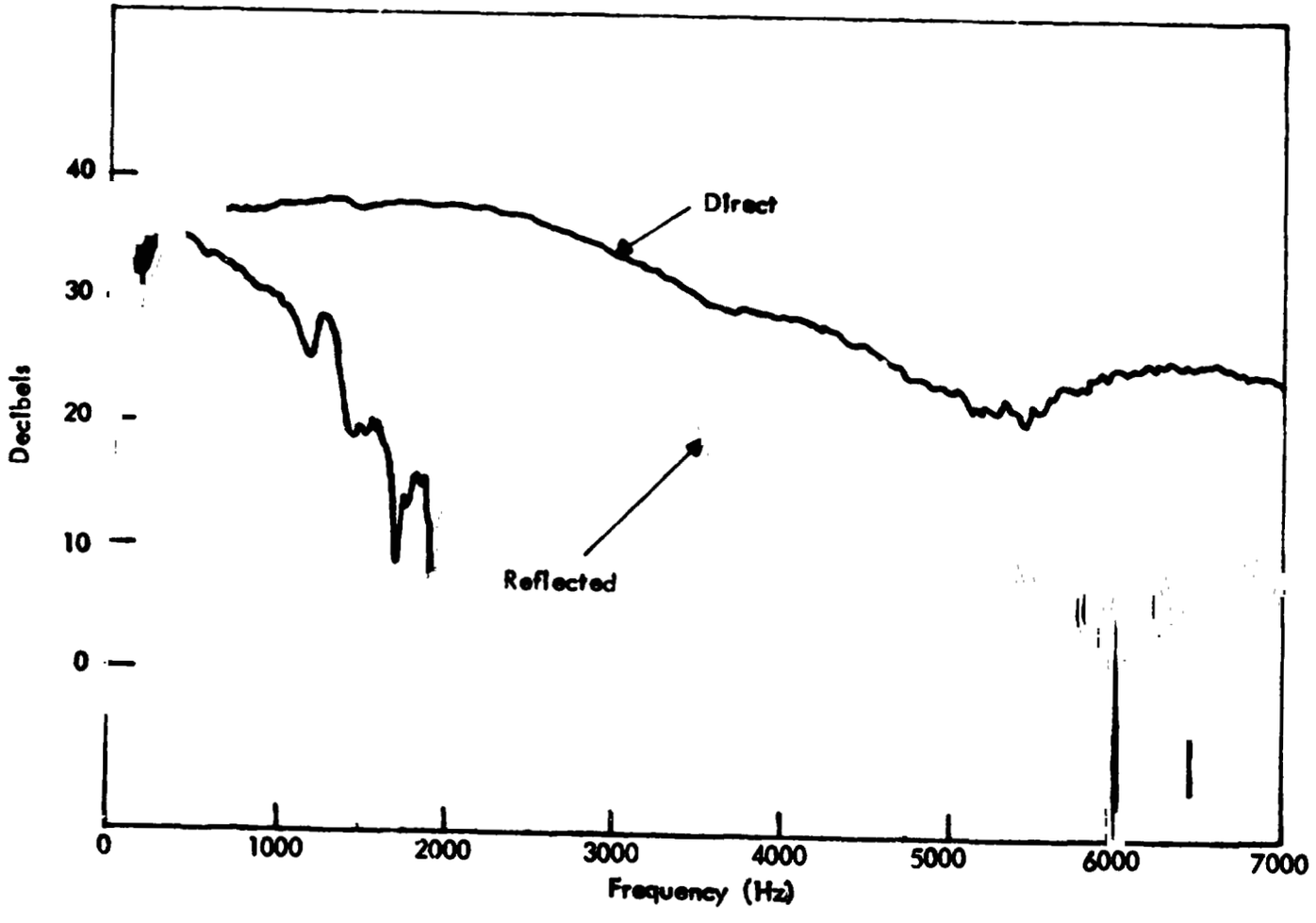

FIGURE 10. SPECTRA OF EDITED TIME HISTORIES OF REFLECTED AND DIRECT PULSES FROM 4" LAYER OF TYPE 701 FIBERGLAS ON TOP OF ASPHALT

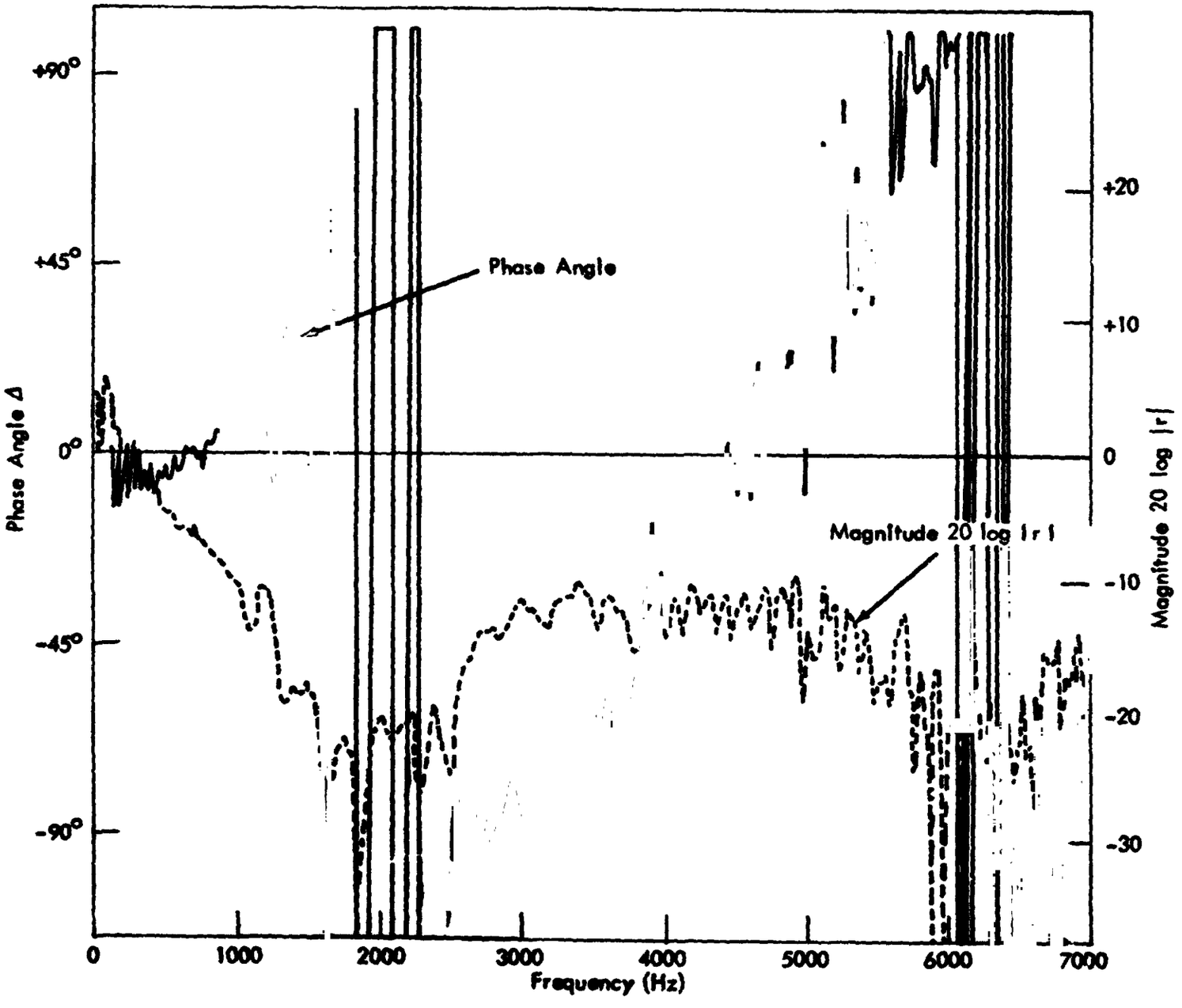

FIGURE 11. MEASURED MAGNITUDE AND PHASE OF REFLECTION COEFFICIENT FROM 4" LAYER OF TYPE 701 FIBERGLAS ON TOP OF ASPHALT

The measured magnitude and phase of the reflection coefficient from the 4-inch layer of fiberglass are shown in Fig. 11. Unfortunately, the range of the plot is such as to indicate phase angles only between -135° and +100°. However, at phase angles outside this range the phase seems to be flip-flopping rapidly, suggesting that the phase is ±180°, a value which will be used in computations when the phase is outside the range in Fig. 11. The impedance of the fiberglass layer is computed from the reflection coefficient using Eq. 2

$$\bar{Z} = \bar{R} - i\bar{X} = \frac{1 + r}{1 - r}, \qquad r \equiv |r|e^{i\Delta} \tag{2}$$

where the barred quantities indicate the sample impedance quantities normalized by the acoustic impedance ρc, and $|r|$ and Δ are the magnitude and phase angle of the reflection coefficient, respectively. Equation 2 is compatible with the notation that the time dependence is $e^{-i\omega t}$ and positive reactance is a mass, whereas a negative reactance is a stiffness. Alternately, the normalized impedance can be calculated from charts such as those given in Reference 2.

The magnitude and phase angle measurements shown in Fig. 11 are tabulated in Table 1. Because the 4-inch layer of fiberglass was located above the ground plane which was used as a reference in locating the source and the microphones, it is necessary to correct the measured phase angle of the reflection coefficient in order to calculate the impedance referenced to the fiberglass upper plane. The phase angle must be corrected by the amount of phase change associated with the wave traveling twice the thickness h of the fiberglass layer as in Eq. 3:

TABLE I

IMPEDANCE CALCULATION (4" Layer Fiberglass)

Freq.	Magnitude of Reflection Coeff.		Phase Angle of Reflection Coeff.			Impedance Measured		Impedance Calculated	
	20 log |r|	|r|	Raw Δ	Layer Corr.δ	Corr.Δ	$\bar{R}$	$\bar{X}$	$\bar{R}$	$\bar{X}$
250	- 2 dB	0.79	- 6°	+ 54°	300°	0.4	-1.6	.8	-2.1
500	- 3 dB	0.71	- 4°	+107°	249°	0.3	-0.7	.8	-1.0
1000	-11 dB	0.28	+ 13°	+214°	159°	0.5	+0.15	.8	-0.5
2000	-20 dB	0.10	± 180°	+ 68°	112°	0.9	+0.15	.8	-0.25
4000	-12 dB	0.25	- 26°	+136°	198°	0.6	-0.10	.8	-0.1
6000	-21 dB	0.09	± 180°	+204°	336°	1.2	-0.10	.8	-0.05

$$\delta = 360° \frac{2h}{\lambda} = 0.214°f. \qquad (3)$$

To deduce the sign of the phase correction, assume that we had oriented Microphone A, shown in Fig. 1, 8 inches closer to the ground plane so that the direct path would equal that of a reflection off the fiberglass upper surface. At the instant the reflected pulse arrived at Microphone B, the lowered Microphone A would have a phase angle increased by the amount given in Eq. 3 over that actually recorded at Microphone A. Thus we must add the phase-angle correction to Microphone A or, since the coefficient is the ratio of B to A, subtract the correction given in Eq. 3 and tabulated in Table 1 from the raw data presented in the table. Finally, the impedance values calculated from Eq. 2 or the referenced charts using the reflection coefficient magnitude and corrected phase data shown in Table 1 are presented in the last two columns of the table.

These measured values are also compared in the table with the values computed for the 4-inch fiberglass layer using Eqs. 4 and 5.

$$\overline{R} = \frac{R_1 h}{\rho c} = \frac{10^4 \text{ MKS Rayls/m. x } 0.1\text{m}}{3 \text{ x } 407 \text{ MKS Rayls}} = 0.8 \qquad (4)$$

$$\overline{X} = \frac{-\lambda}{2\pi h} = \frac{-535}{f} \qquad (5)$$

The measured and calculated impedance values shown in Table 1 are in qualitative agreement, but there some noticeable discrepancies. The measured resistance values are low at low frequencies

and high at high frequencies compared to the Eq. 3 calculation which assumes that one-third of the total resistance is effective at all frequencies. A more detailed calculation of the effective resistance is the value of $v^2 = \sin^2(X/\lambda)$ averaged over the layer depth. This simple calculation yields effective resistance values of 0.5 at 250 Hz and 1.2 at frequencies of 500 Hz and above. Thus there is considerable uncertainty concerning the appropriate resistance calculation.

The discrepance between measured and calculated reactance at 250 and 500 Hz can be explained as follows. At low frequencies, the acoustic compressions in a fiber-filled layer are isothermal rather than adiabatic, because of heat transfer to the fibers. The effective stiffness is therefore reduced by the factor $\sqrt{1.4} = 1.2$ which yields calculated stiffness values of -1.75 at 250 Hz and -0.8 at 500 Hz.

The pulse reflection technique was also used to measure the impedance of the bare asphalt ground plane, and the raw reflection coefficient data are shown on Fig. 12. At a frequency of 3000 Hz, the magnitude and phase of the reflection coefficient shown in Fig. 12 are 0.67 and -20°, respectively, which translate to an impedance of $\bar{Z} = 3 - 2.5i$. Limited available information on the impedance of asphalt ground surfaces suggests that at a frequency of 3000 Hz the normalized impedance might be $\bar{Z} = 5 - 2i$, which translates back to a reflection coefficient magnitude and phase angle of 0.7 and -10°, respectively.

It is informative to explore the errors in the calculated impedance due to uncertainties in the reflection coefficient phase angle caused in turn by uncertainties in the source and microphone positions described by Eq. 1. Figure 13 shows the impedance

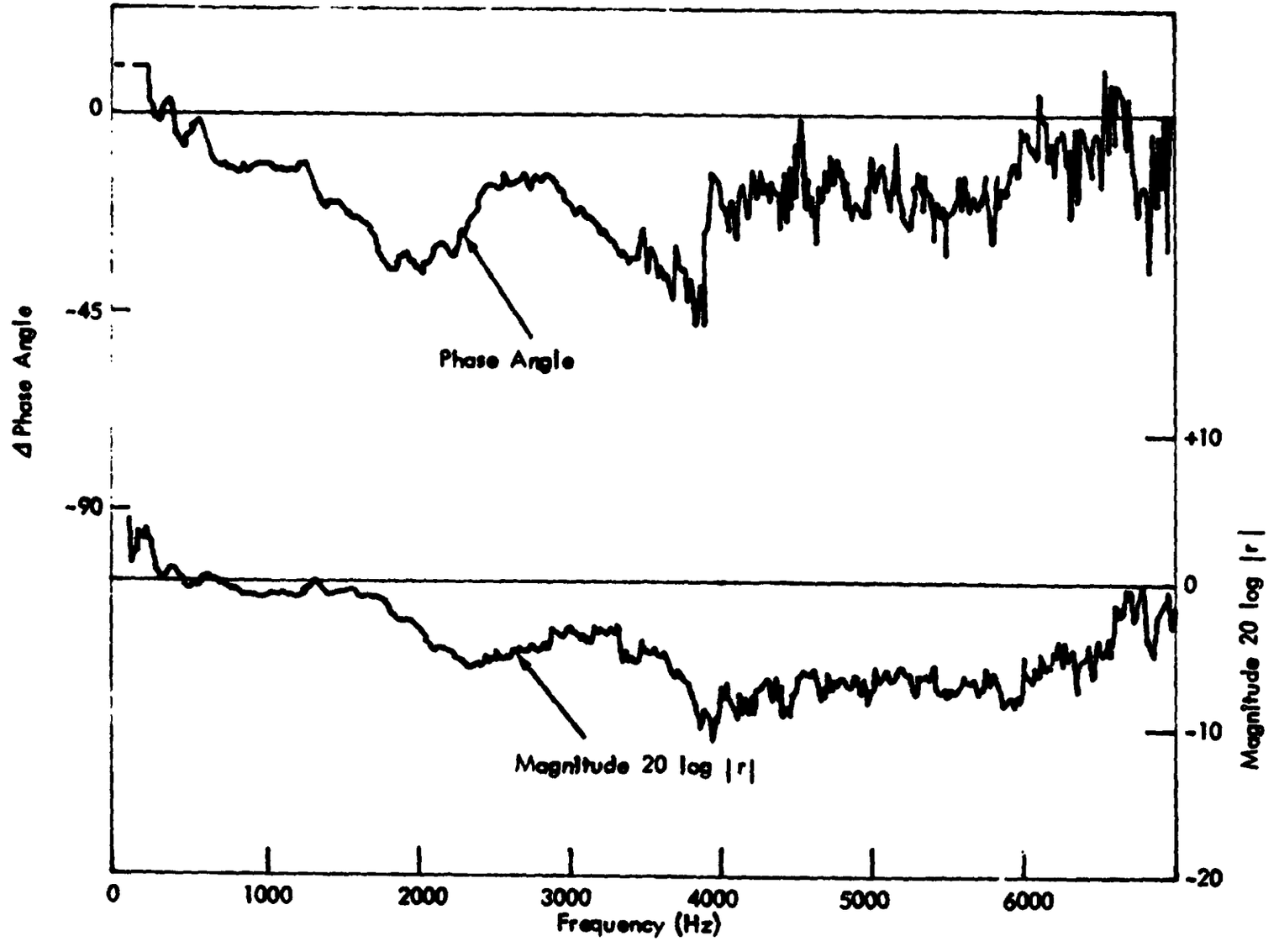

FIGURE 12. MEASURED MAGNITUDE AND PHASE OF REFLECTION COEFFICIENT FROM ASPHALT

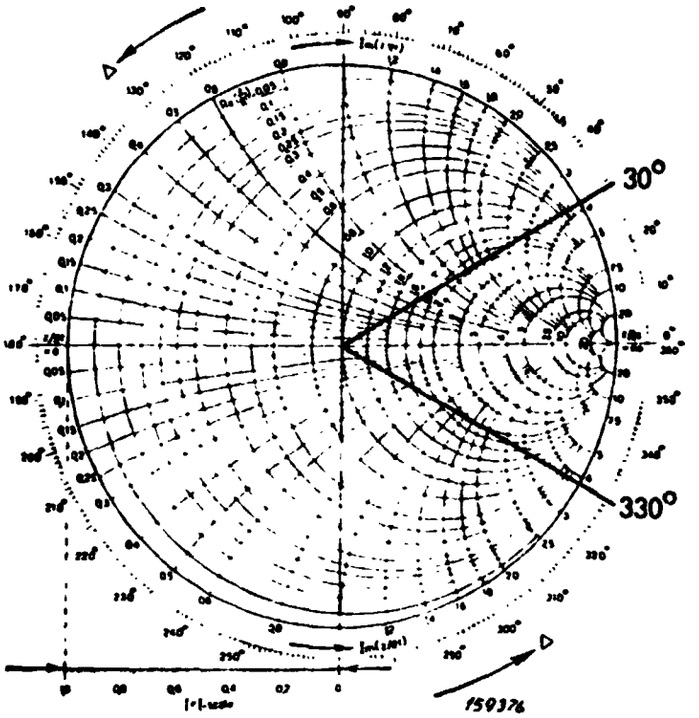

(a) ± 30° Effect on High Impedance

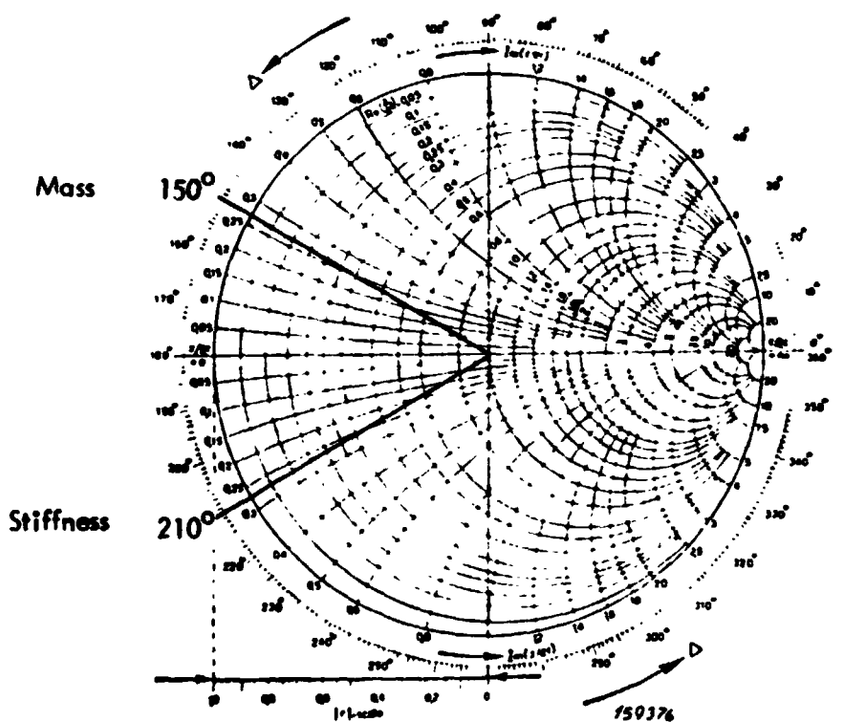

± 30° Effect on Low Impedance

FIGURE 13. IMPEDANCE UNCERTAINTY RESULTING FROM ±1cm. DISTANCE UNCERTAINTY AT 3000 Hz (PHASE ANGLE Δ = ± 30°)

uncertainty resulting from a ±1 centimeter distance uncertainty at 3000 Hz, which results in a phase angle uncertainty of ±30°. Figure 13(a) indicates that, for a high impedance surface such as the asphalt ground plane, a ±30° uncertainty in the reflection coefficient phase angle for the case of 0.7 magnitude yields a range of resistances $2 < R < 6$ and reactances $-3 < X < +3$. Alternately, Fig. 13(b) indicates that for a low impedance sample, an uncertainty in the reflection coefficient phase angle of ±30° for a 0.7 magnitude yields a range in resistances of $0.17 < R < 0.19$ and of reactances of $-0.3 < X < +0.3$.

Measurements of the magnitude of the reflection coefficient are subject to less errors than the phase. A recent report describes a similar measurement technique which uses a single microphone and a broadband random noise source, for measuring only the absorption (Reference 3), and which yields reflection coefficients within ±10%. Possible sources of error in measuring the magnitude of the reflection coefficient include signal-to-noise problems for very absorptive samples where the reflected wave is very small compared to the direct wave; and the aforementioned errors due to editing which can delete significant portions of the pulse energy, particularly in the low frequency regime where significant information is contained in the tails of the pulse.

These experiments confirm the feasibility of the pulse reflection impedance measurement technique, but additional experimentation is required in order to quantify the bias and random errors and to further refine the technique.

2.0 IMPEDANCE TUBE TESTS

An impedance tube was used to quantify the acoustical properties of a number of candidate materials for the 80 x 120 foot wind tunnel mufflers. A conventional Brüel and Kjaer 4-inch diameter impedance tube was used to measure the properties of the candidate fiberglass configuration, and a specialized setup using the same apparatus with an open-end exposed to grazing flow was used for candidate perforated plate muffler materials. Herein the specialized measurement and analysis techniques utilized in the experiments are described, and then the impeddance data are presented and compared with the available theory.

2.1 Measurement and Analysis Techniques

2.1.1 Data Analysis

Figure 14 illustrates the basic impedance tube instrumentation and measurements used in these experiments. The B&K standing wave apparatus Type 4002 was used in conjunction with a sine-wave generator and power amplifier for excitation, and a sound level meter and SD 360 narrow-band analyzer for analysis. The FFT narrow-band analyzer greatly simplifies the use of the impedance tube since, used in the single channel configuration, the analyzer provides 1024 narrow-band filters which may be spread across the frequency range of interest--in our case 0 to 2000 Hz. The 60 dB of resolution provided by each of these filters filters eliminates some of the conventional impedance tube measurement problems such as harmonic speaker and probe distortions.

Figure 14(b) is a schematic of an incident and reflected wave impinging upon the sample end of the tube. The four quantities

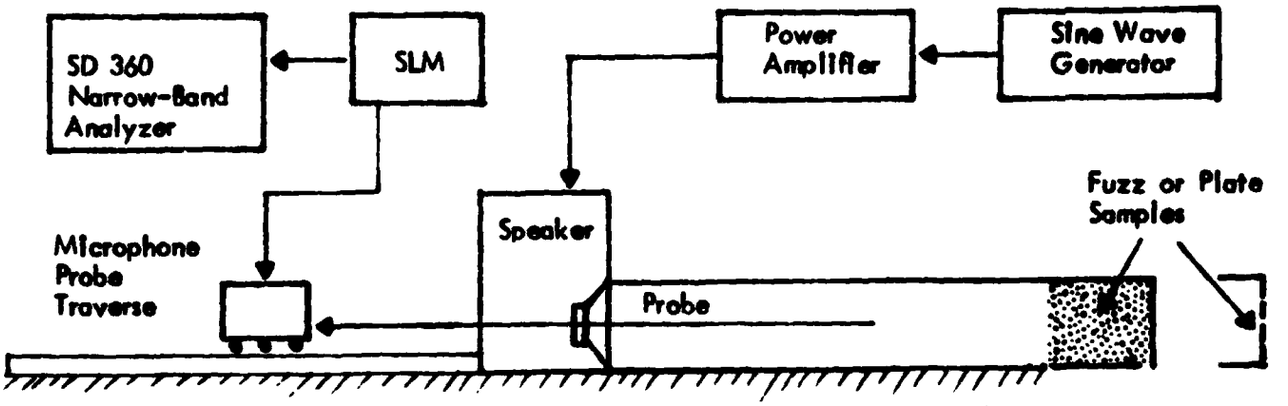

(a) Instrumentation

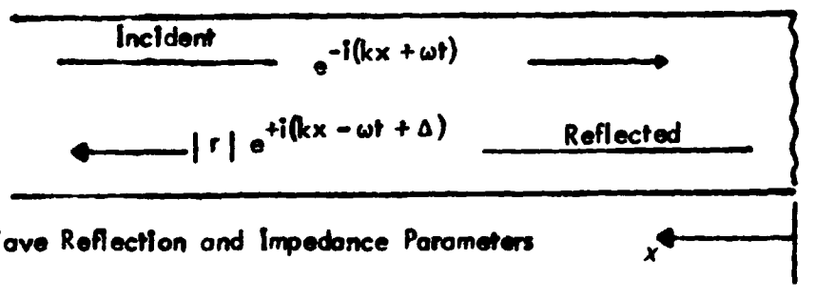

$Z_{end} = \text{Tanh}\,\pi(\alpha - i\beta)$

(b) Wave Reflection and Impedance Parameters

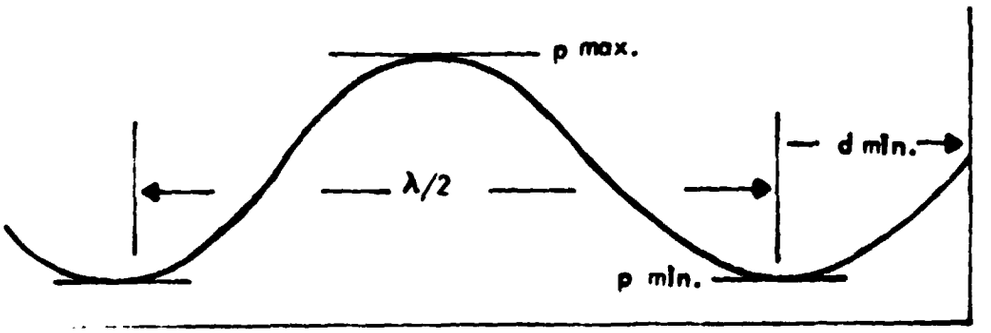

(c) Standing Wave Measurements

FIGURE 14. IMPEDANCE TUBE SET-UP

actually measured in each of the impedance tube tests are illustrated in Figure 14(c): the distance from the sample end of the tube to the first minimum, d_{min}; the sound pressure at the first minimum, p_{min}; the sound pressure at the first maximum, p_{max}; and the half wavelength of the standing wave measured between two successive standing minima.

We investigated two methods of calculating the impedance from these measured quantities. The first method employs the technique set forth in the B&K instruction manual by which these measured parameters are used to calculate the magnitude $|r|$ and phase angle Δ of the reflected wave, Fig. 14(b), according to the formula:

$$|r| = \frac{p_{max}/p_{min} - 1}{p_{max}/p_{min} + 1} \qquad (6)$$

$$\Delta = \left[\frac{d_{min}}{\lambda/4} - 1\right]\pi \qquad (7)$$

where the ratio p_{max}/p_{min} usually expressed in decibels is called the standing wave ratio. Two charts are available in the B&K manual for calculating the real and imaginary parts of the sample impedance from the reflection coefficient magnitude and phase angle (one of these types of charts is shown in Fig 13).

In this study, for more accuracy we used an alternative technique based on the analysis presented in Reference 4. Thereby the sample impedance is expressed in terms of the wave propagation parameters α and β described by the equation in Fig. 14(b), which is conveniently evaluated by means of plate 1 of Reference 4. These wave propagation parameters

are related to the measurement properties shown in Fig. 14(c) by the following relations:

$$\alpha = \frac{1}{\pi} \tanh^{-1}(p_{min}/p_{max}) \quad (8)$$

$$\beta = 1 - \frac{2\, d_{min}}{\lambda} \quad (9)$$

Plate 1 of Reference 4 is also used to evaluate α given by Eq. 8.

2.1.2 Grazing Flow Test Configuration

The test setup for measuring the impedance of perforated plates with grazing flow is shown in Fig. 15. The sample was mounted in the open end of the 4-inch diameter tube and a 6:1 aspect ratio nozzle was positioned adjacent to a half-inch thick plywood collar at the end of the tube. Air was supplied in a blow-down mode from large tanks with two quiet valves used to regulate the upstream total pressure p_o to control the exit velocity V. The tests were run with nine different velocities involving nozzle total pressures ranging from 0 to 5.85 inches of water and nominal exit velocities from 0 to 160 ft/sec as indicated in Table 2.

TABLE 2
GRAZING FLOW VELOCITIES

Run No.	1	2	3	4	5	6	7	8	9
Δ in. H_2O	.00	.04	.24	.69	1.38	2.3	3.29	4.48	5.85
V nominal [ft/sec]	0	11	33	55	77	99	120	140	160
V average [ft/sec]	0	8	24	40	55	71	86	101	115

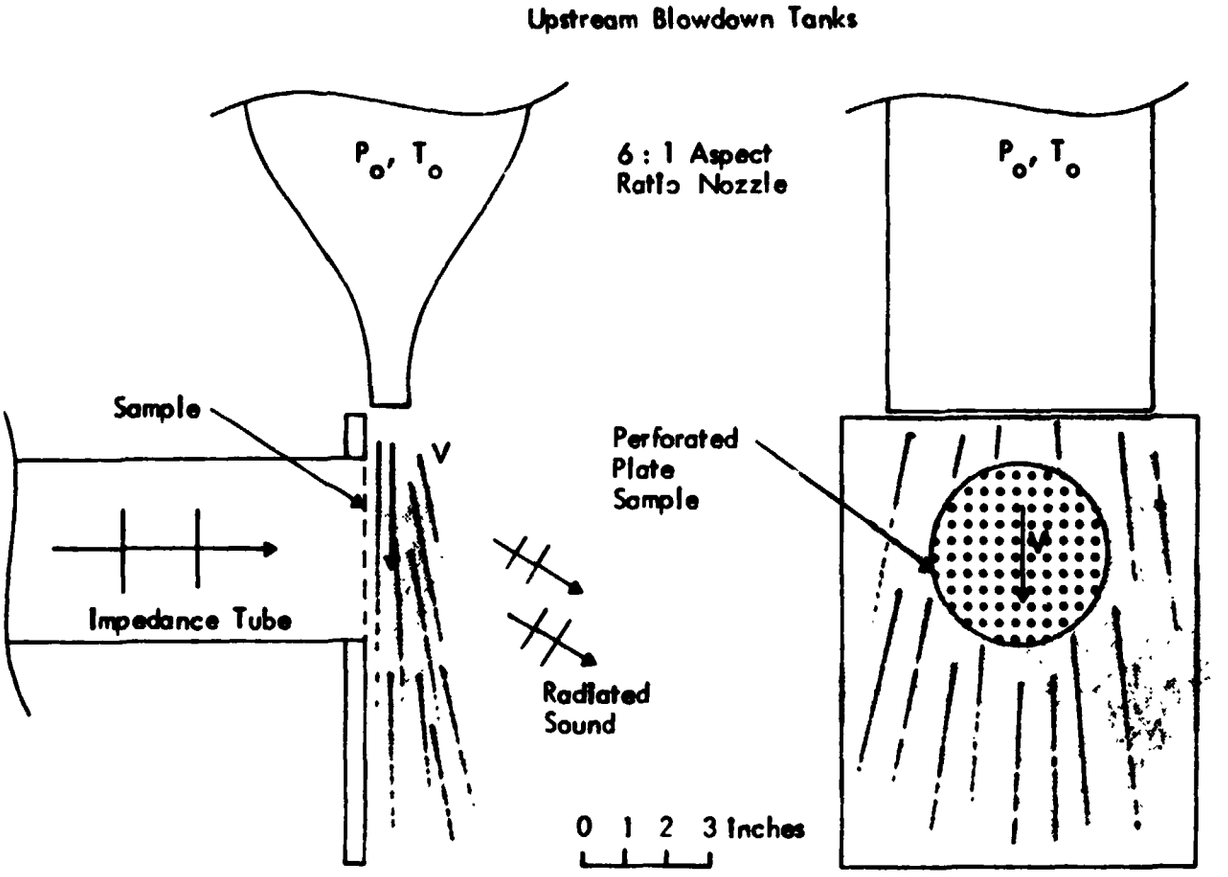

(a) Set-up of Open End Tube With Transverse Flow

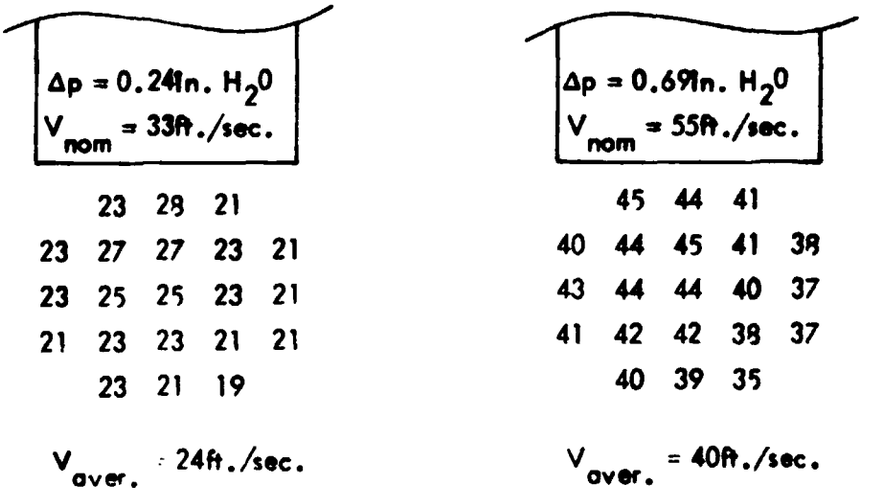

(b) Measured Velocity Profiles on Plate Surface

FIGURE 15. FLOW CONFIGURATION FOR PERFORATED PLATE IMPEDANCE MEASUREMENT

Figure 15(b) shows velocity profiles measured on the perforated plate face for the two conditions of V nominal equal 33 and 55 ft/sec. The calculated average velocities on the plate for these two conditions were 24 and 40 ft/sec, respectively. On the basis of these data, the nominal velocities in Table 2 were discounted by the factor 0.72 to yield the average velocities used in presenting the impedance data.

2.1.3 Combined Impedance Analysis

The impedance and therefore the acoustical performance of a built-up muffler is the net effect of several constituent parts of the configuration. Similarly, in an impedance tube the effective impedance at the end of the tube may be due to several components. The diagram in Fig. 16(a) describes this situation for the case of a 5 inch slug of fiberglass mounted at the end of a closed impedance tube. Here the primary two elements in the frequency range from 0 to 2000 Hz are the resistance of the fiberglass and the stiffness of the 5-inch air column. In this configuration, as in the candidate fiberglass muffler configuration without a facing material, the effective impedance is simply the sum of the fiberglass resistance and the air column stiffness reactance.

The situation in the impedance tube measurement of the perforated plate with grazing flow, illustrated in Fig. 16(b), is somewhat peculiar, in comparison to the candidate perforated plate muffler configuration. In the impedance tube experiment the measured net impedance Z is the sum of the perforated plate impedance Z_p and the radiation impedance Z_{rad} for the end of the tube. Both the plate impedance and the radiation impedance have resistive and mass reactive components. On the basis of the analysis in Fig. 16(b), demonstrating that the impedances

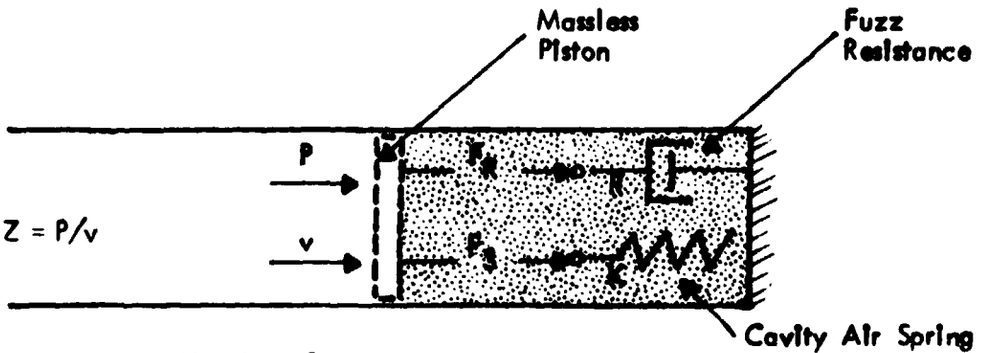

$PA = F_R + F_S$

$Z = R + jK/(\omega A)$

(a) Closed Tube Summation of Fuzz Resistance and Cavity Stiffness

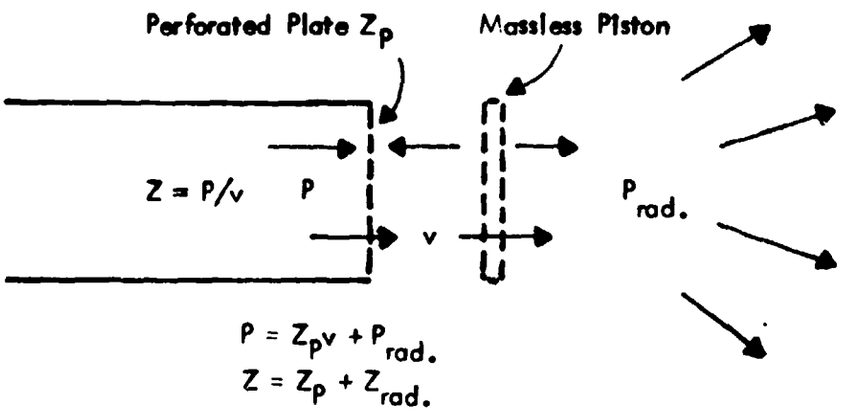

$P = Z_p v + P_{rad.}$

$Z = Z_p + Z_{rad.}$

(b) Open Tube Summation of Perforated Plate and End Radiation Impedance

FIGURE 16. ANALYSES OF COMBINING IMPEDANCES FOR THE CLOSED AND FOR THE OPEN END TUBE EXPERIMENTS

are simply additive, the plate impedance is calculated by subtracting the adiation impedance measured with the plate removed from the net impedance measured with the plate in position. The measured radiation impedances are compared in Table 3 with theoretical values for a baffled and unbaffled piston taken from Reference 5. The measured reactances are in good agreement with the theoretical values for a baffled piston, as are the measured resistances at 500 and 1000 Hz. At 125 and 250 Hz the measured resistances are more comparable to the unbaffled theory. In all cases the measured resistance and reactance values were used to correct the measured net impedance.

TABLE 3
RADIATION IMPEDANCES

	Measured		Theoretical Baffled		Theoretical Unbaffled	
Frequency	R	X	R	X	R	X
125	.003	.10	.015	.10	.01	.06
250	.016	.20	.03	.21	.016	.1
500	.08	.40	.12	.40	.09	.34
1000	.35	.70	.37	.61	.21	.46

2.2 Results

2.2.1 Theoretical Values

The analyses for the resistance and stiffness of the fiberglass configuration are described by Eq. 4 and 5 and the ensuing discussion in Sec. 1.

For the perforated plate, the resistance must be studied in two regimes: a linear regime where resistance depends only on the plate properties, and a nonlinear regime where the resistance is linearly proportional to the grazing flow velocity. In the linear regime the porous perforated plate resistance is given (Reference 6) by Eq. 10:

$$R = \frac{(8\mu\rho 2\pi f)^{\frac{1}{2}}}{F}(1 + t/d) = 0.034 f^{\frac{1}{2}}(1 + t/d) \qquad (10)$$

where μ is the fluid viscosity, ρ the density, f the frequency, t the plate thickness, d the hole diameter, and F the perforated plate fraction open. Equation 10 applies for a single hole when F is taken equal to unity.

In the nonlinear regime the perforated plate resistance is given by the very simple relation:

$$R = \frac{0.67}{F}\rho V \qquad (11)$$

where V is the grazing flow velocity. It is interesting to note that in the nonlinear regime the flow resistance depends only on the fraction open of the plate and not on the hole diameter or plate thickness. It has been known for some time that in the nonlinear regime the resistance is equal to the product of the density and the velocity through the hole (Reference 6), but the importance of grazing flow and the constant of proportionality in Eq. 11 have only recently been recognized, Reference 7. The constant of proportionality in Eq. 11 was determined here (crudely) by averaging the constants of proportionality for plus and minus acoustic half cycles involving alternately inflow and outflow through the hole using the results from Reference 7.

The mass reactance of a perforated plate with no flow is given by:

$$X_{mass} = \frac{\rho c}{F} \frac{2\pi}{\lambda} (t+0.85d) \qquad (12)$$

where λ is the acoustic wavelength Reference 8. The effect of grazing flow velocity on the reactance is not well understood but Reference 9 indicates that the reactance value with high grazing flow is one-half the linear value given in Eq. 12. These theoretical values are compared with measured data for the 3% open perforated plate configuration in Figures 20 and 21.

2.2.2 Fiberglass Baseline

Figure 17 shows the calculated and measured impedance of a five-inch slug of Type 701 fiberglass in the closed end of the impedance tube. The calculated resistance and stiffness values are taken from Eqs. 4 and 5, respectively. The measured stiffness values agree closely with the calculated stiffnesses and do not show the isothermal effect discussed in Section 1. The measured resistances, however, do not agree well with the value calculated from the steadystate flow resistance but rather increase with frequency over the range from 125 to 1000 Hz. (The data point at 2000 Hz is somewhat suspect because at this point the four-inch diameter impedance tube has several cross modes.) The measured increase in resistance with frequency is similar to that observed with the pulse reflection measurement of the fiberglass blanket described in Section 1.

The measured resistance and reactance of the five-inch slug of Type 701 Fiberglas is in close agreement at a frequency

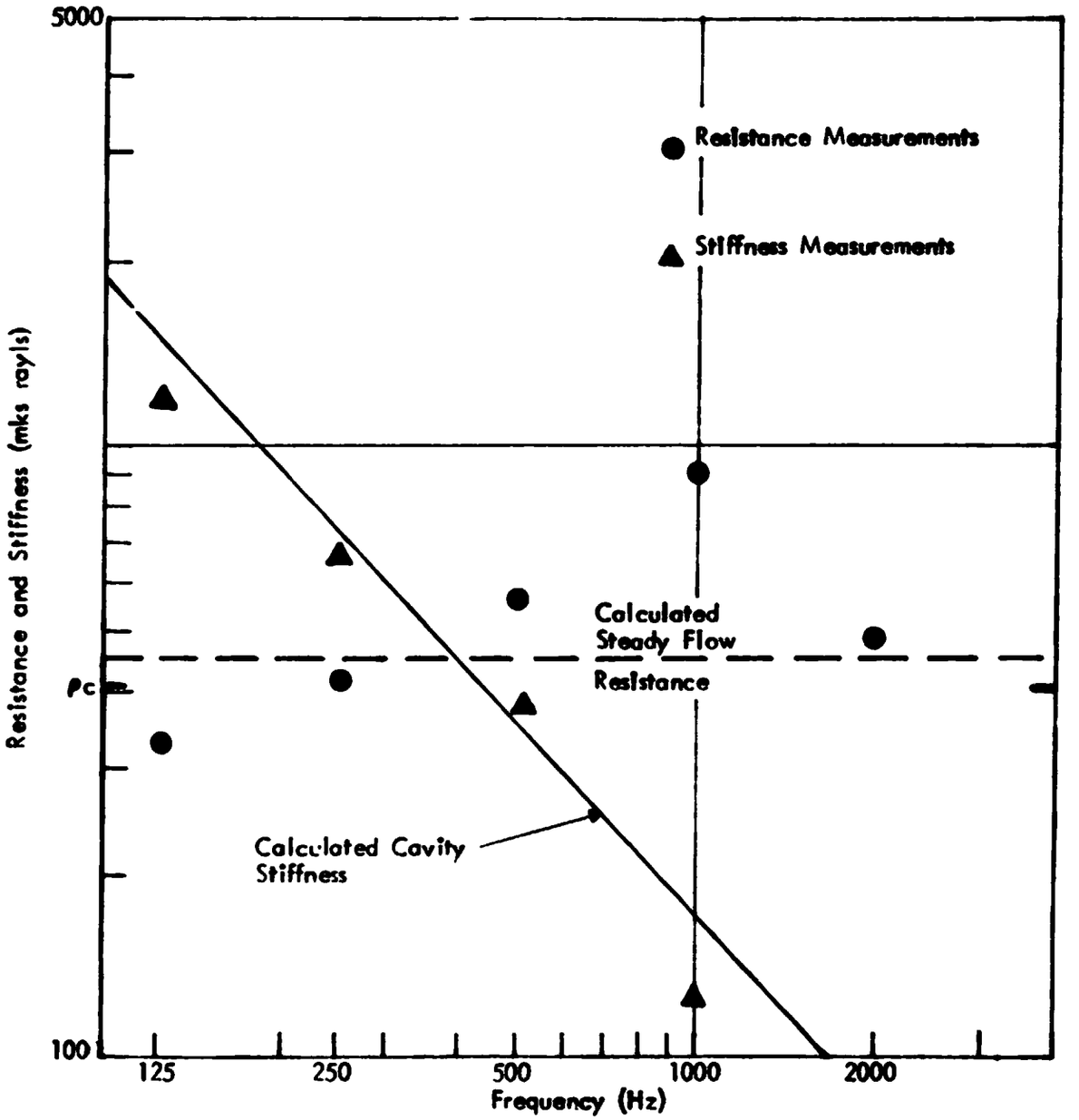

FIGURE 17. IMPEDANCE OF 5 INCH SLUG OF TYPE 701 FIBERGLAS IN CLOSED END TUBE

of approximately 500 Hz with the theoretical optimum impedance for maximum sound absorption (Reference 10):

$$Z_{optimum} = (0.92 - 0.77i)\frac{2h}{\lambda} \qquad (13)$$

where h is the half duct width equal to one foot in the case of the baseline 80 x 120 foot wind tunnel muffler design. In addition the resistance increases with frequency, as desired, but is not proportional to frequency as is required by Eq. 13. In practice it is good to design for resistance values somewhat higher than the optimum value which yields a phenomenal attenuation of 19 dB per half duct width, in order to obtain broader band performance. Unfortunately, as with all muffler configurations involving a tuned cavity, the stiffness decreases with frequency rather than increases with frequency as required by Eq. 13

2.2.3 Fiberglass Cloth

Because fiberglass cloth is often used as facing to protect fiberglass mufflers against low velocity flows, we have measured and presented in Figs. 18 and 19 the resistance and reactance, respectively, of a commonly used fiberglass cloth, Style 126, for various grazing flow velocities, using the open end impedance tube configuration shown in Fig. 15(b). Both the resistances and the reactances of the fiberglass cloth for the range of flow velocities tested are approximately 10% of the values for the five-inch fiberglass slug presented in Fig. 17. The cloth resistances will add to those of the fiberglass slug, but the reactances will subtract, since the cloth reactances are mass and those of the slug are stiffness.

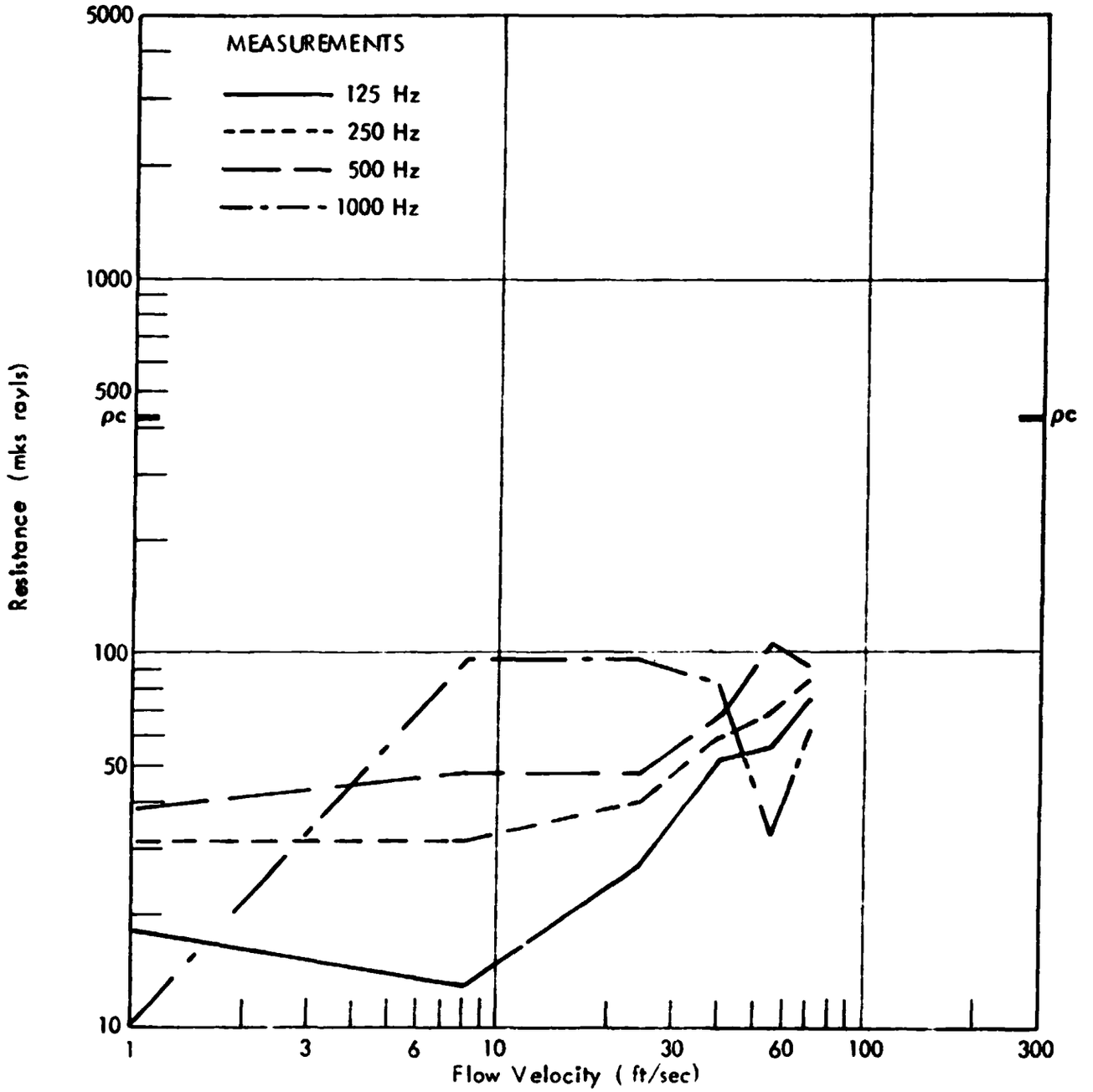

FIGURE 18. RESISTANCE OF FIBERGLAS CLOTH STYLE 126

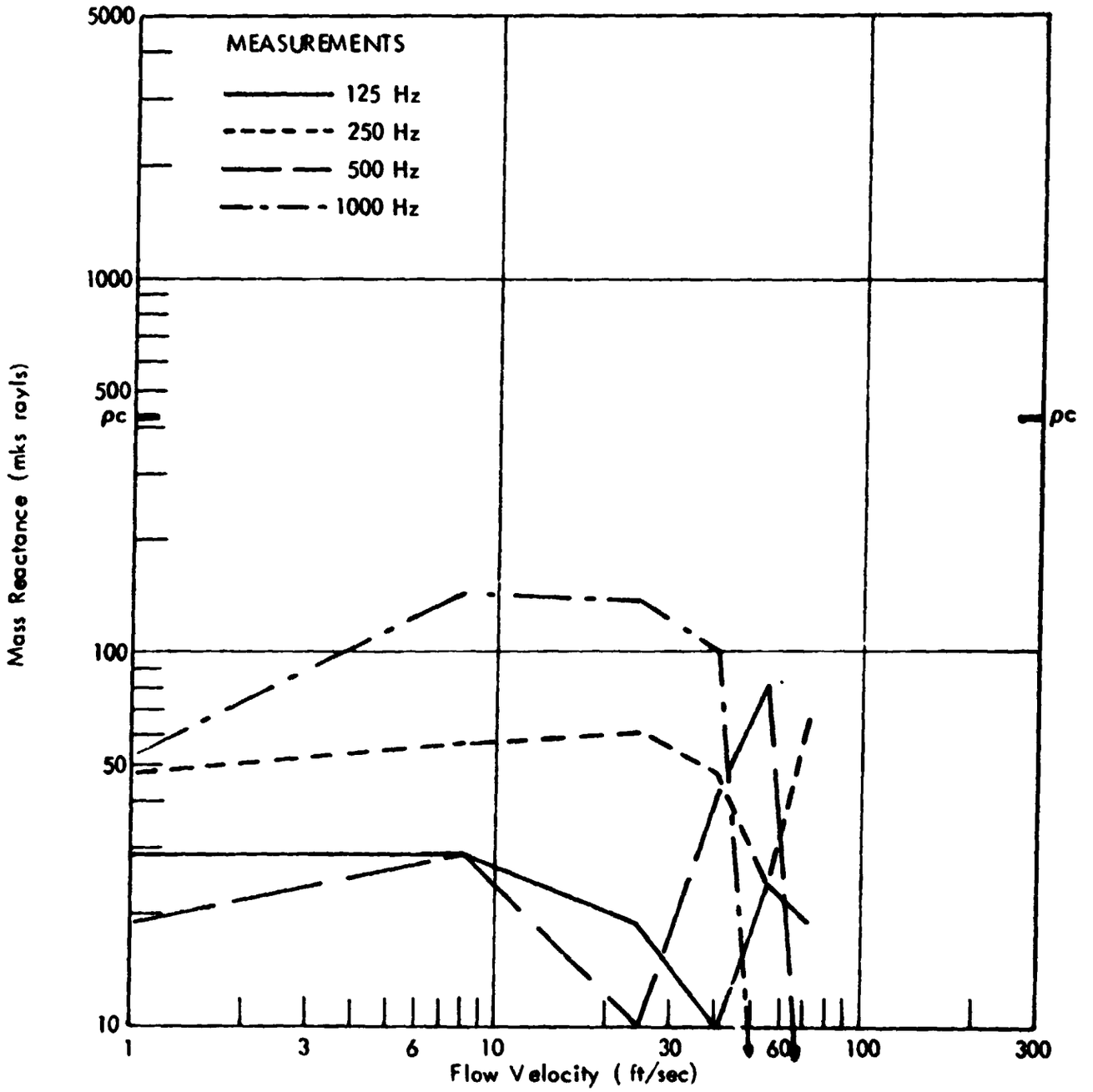

FIGURE 19. REACTANCE OF FIBERGLAS CLOTH STYLE 126

2.2.4 Three-Percent Open Perforated Plate

Figures 20 and 21 show the measured values of resistance and reactance of the 3% open perforated plate recommended for the baseline design for the 80 x 120 foot wind tunnel inlet and exhaust silencers. Also shown are the theoretical impedance values given by Eqs. 10 through 12. Resistance values shown in Fig. 20 agree well with the theoretical predictions except that the nonlinear values are approximately 10 to 20 percent lower than theory depending on the velocity range. This may be due to uncertainty in the proportionality factor of Eq. 11 or perhaps may be associated with the vena contracta effect reducing the effective hole size and therefore the fraction open of the plate.

The resistance values at frequencies of 125 to 1000 Hz and at the velocities appropriate to maximum fan speed in the inlet, 87 ft/sec. and in the exhaust, 120 ft/sec, are approximately 500 to 800 mks rayls. These resistance values are very comparable to those for the 6 inch layer of fiberglass configuration. At lower velocities than maximum, particularly at zero flow velocity, the resistances are considerably lower than what we desire for optimum performance. This is of concern with respect to silencing test-section model noise since the fan noise itself falls off as 50 log of the wind tunnel velocity.

The measured reactance values of the 3% open perforated plate are again in close agreement with theory as shown in Fig. 21 for velocities below 40 ft/sec. At velocities between 55 and 71 ft/sec the reactance values show a surprising dip, the explanation for which is not available. This phenomenon should be investigated further because it might be advantageous

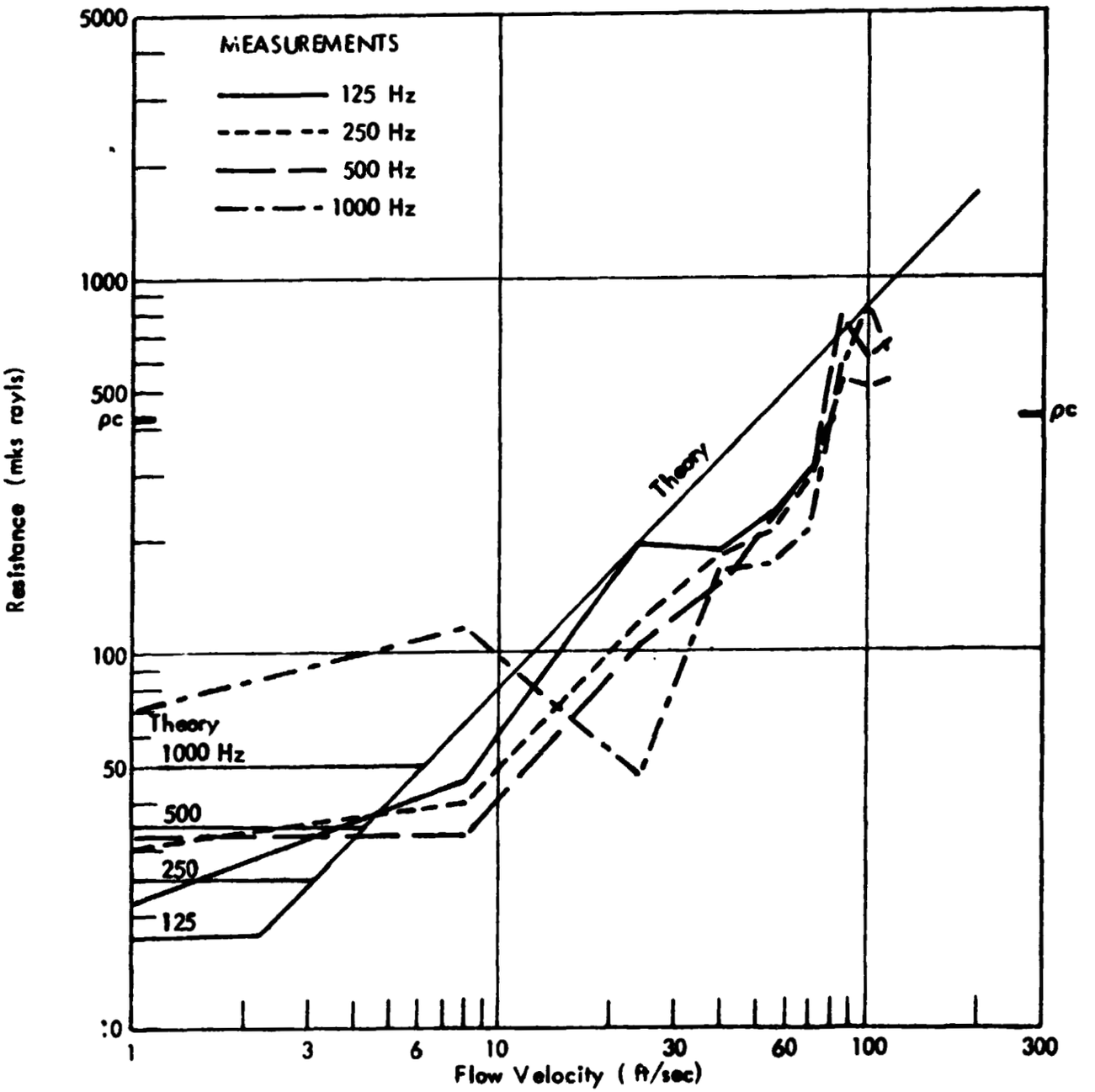

FIGURE 20. RESISTANCE OF 3% OPEN PERFORATED PLATE (0.025 in. thickness and 0.0625 in. hole diam.)

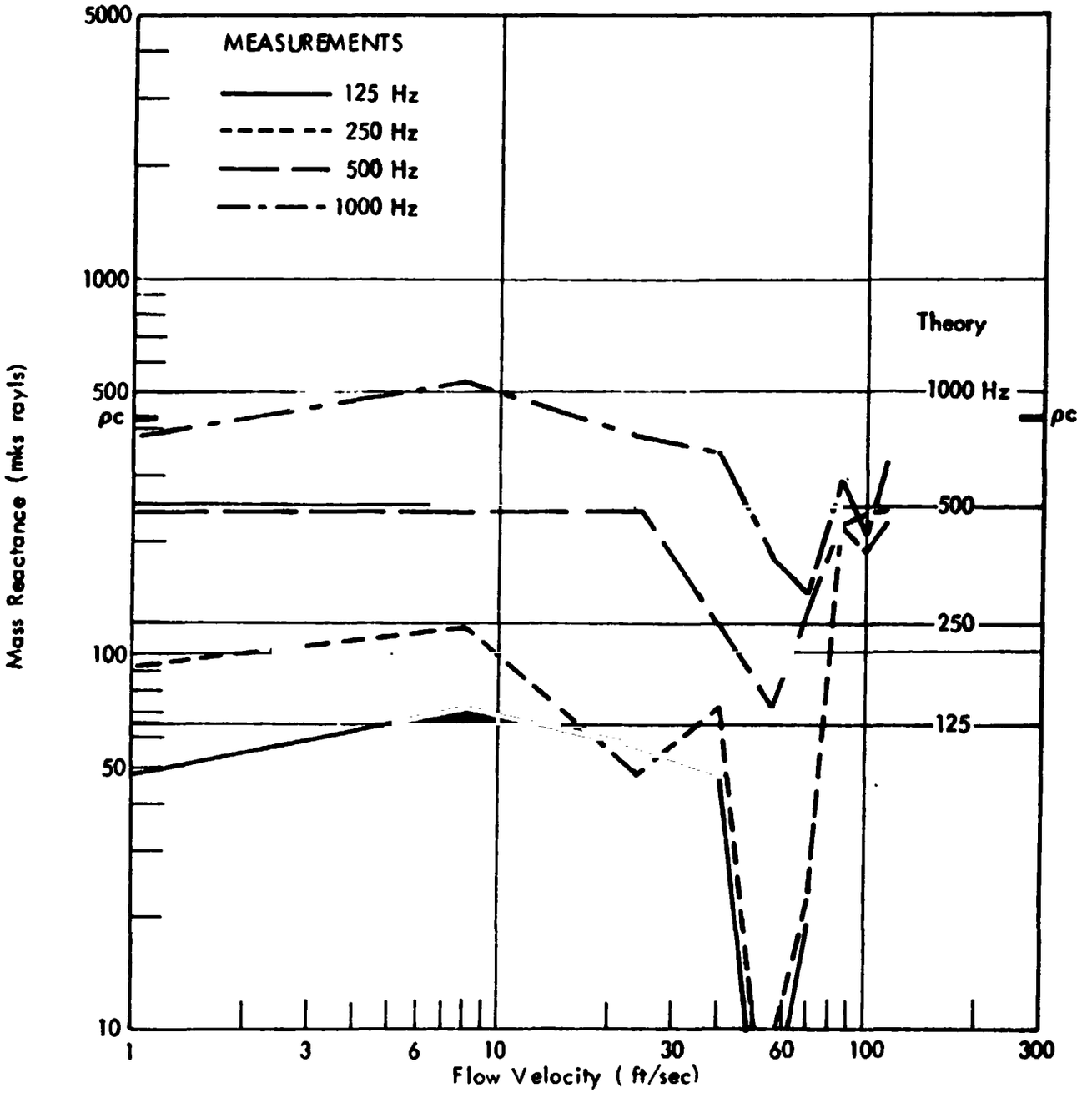

FIGURE 21. REACTANCE OF 3% OPEN PERFORATED PLATE (0.025 in. thickness and 0.0625 in. hole diam.)

if the dip could be moved to the tunnel maximum velocity. Unfortunately at the maximum velocities of interest between 86 and 115 ft/sec, the reactance values, shown in Fig. 21, increase to approximately 200 to 300 mks rayls. Not shown in Fig. 21 is the stiffness reactance which will result when the perforated plate is mounted in the wind tunnel muffler configuration with a 6 inch cavity backing. In this built-up configuration, the stiffness reactance will be like that shown in Fig. 17 and will thus mask or cancel the perforated plate mass reactance at frequencies below 500 to 1000 Hz. Thus the resistance of the built-up perforated plate muffler is predicted to be primarily resistive at frequencies below 1000 Hz. with significant tunnel velocity.

2.2.5 One-Percent Open Perforated Plate

Tests of a 1% open perforated plate obtained by covering with tape 2 of 3 holes of the 3% plate was tested in order to investigate the sensitivity of resistance and reactance to the fractional open area of the plate indicated by Eqs. 10 - 12. As predicted the results shown in Figs. 22 and 23 show that both the resistances and reactances for velocity ranges of interest increase by approximately a factor of three for the 1% open plate.

2.2.6 Three-Percent Open Perforate With Screen

Figures 24 and 25 present the impedance of the 3% open plate plus a 36% open fine brass screen. These measured impedance values are very similar to those obtained with the 3% open perforated plate alone shown in Figs. 21 and 22.

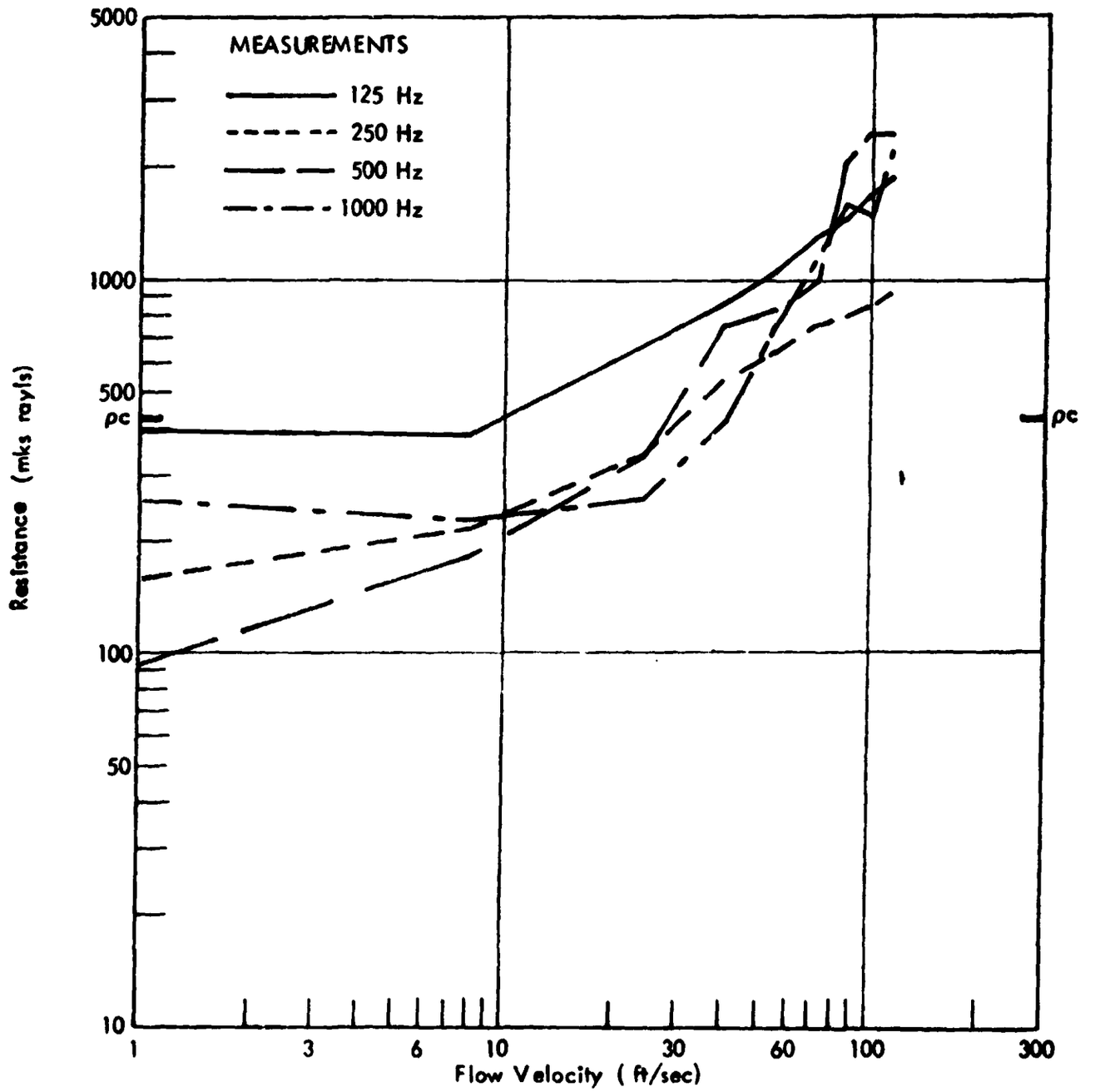

FIGURE 22. RESISTANCE OF 1% OPEN PERFORATED PLATE (0.025 in. thickness and 0.0625 in. hole diam.)

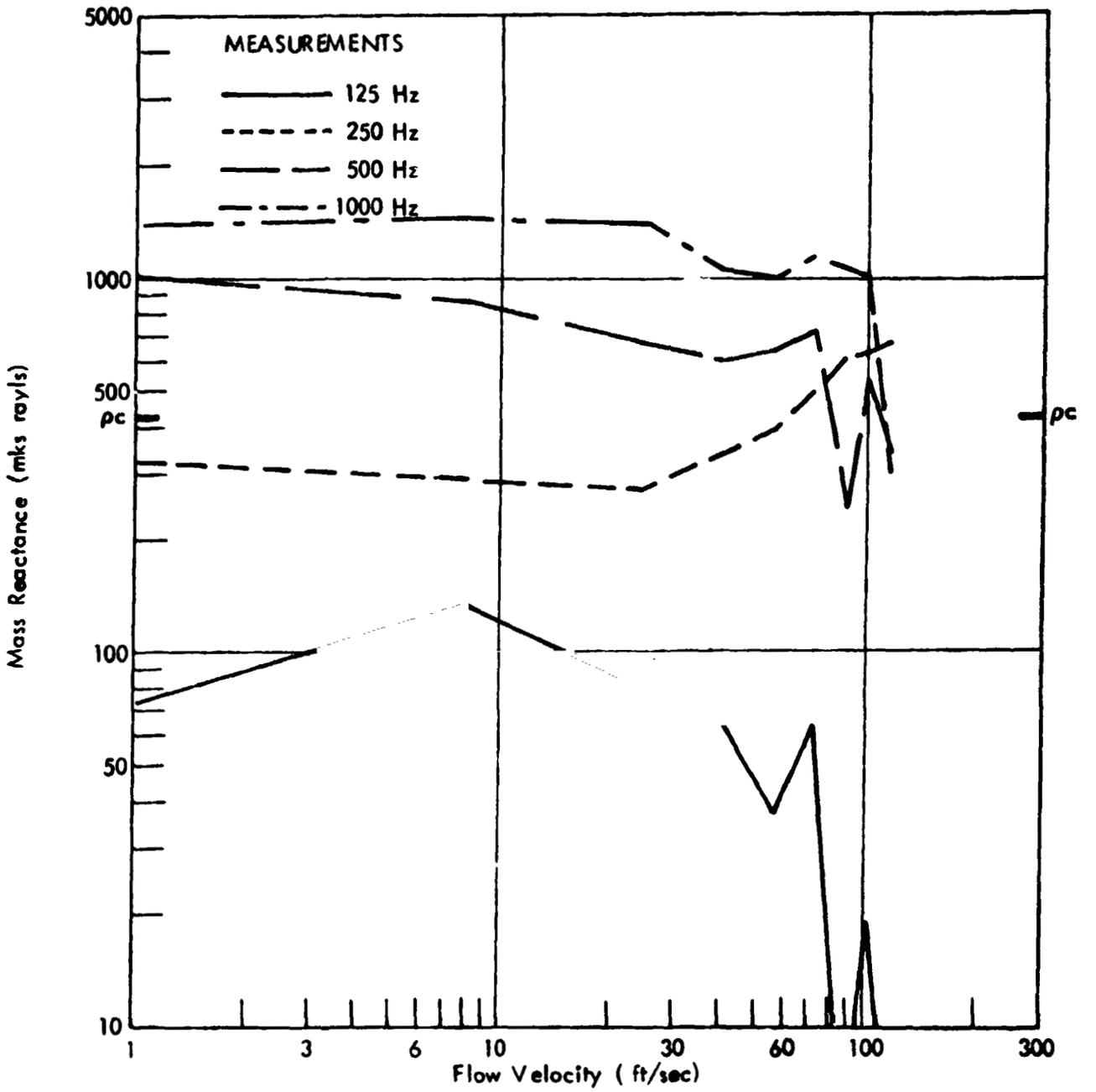

FIGURE 23. REACTANCE OF 1% PERFORATED PLATE (0.025 in. thickness and 0.0625 in. hole diam.)

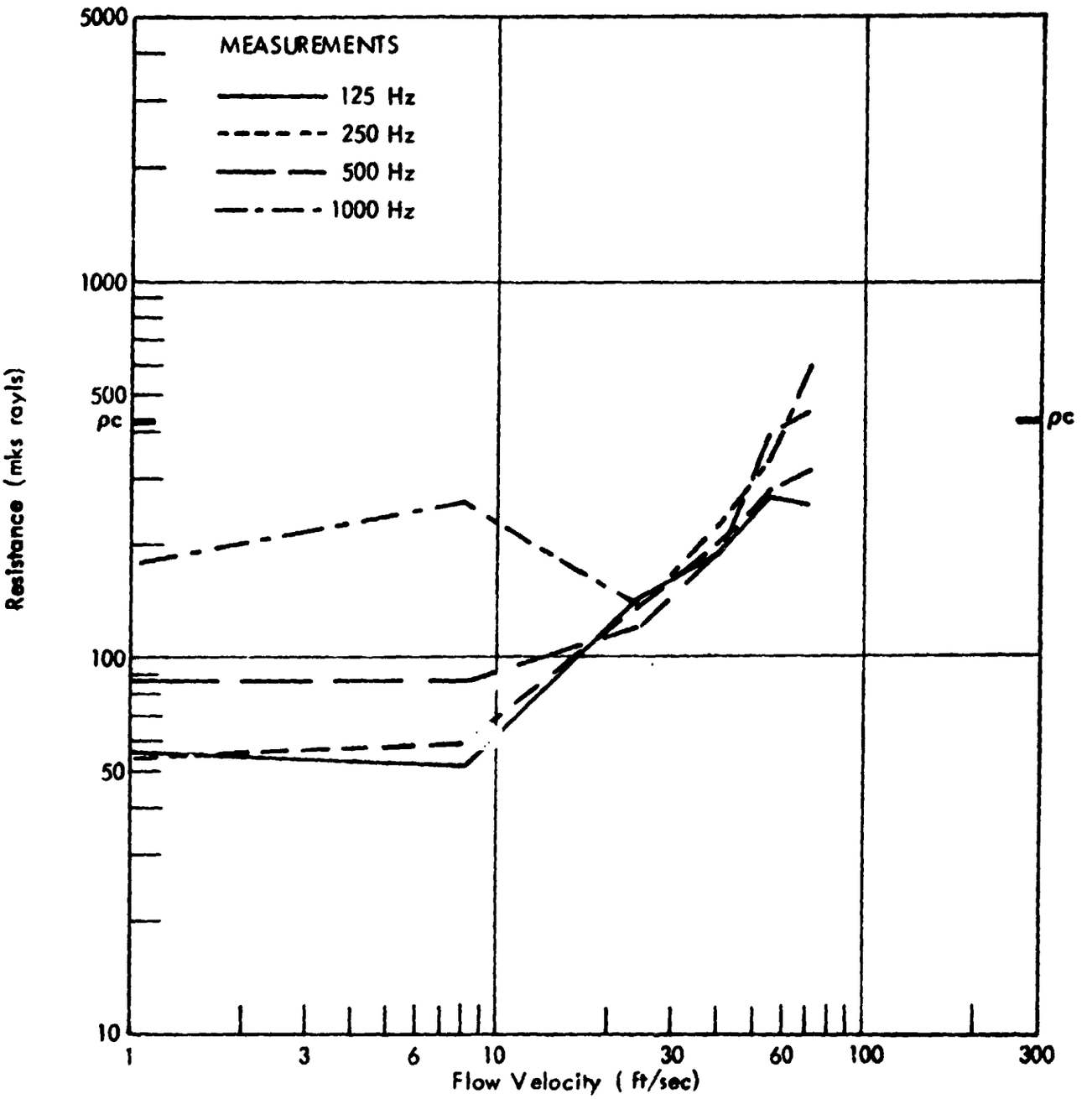

FIGURE 24. RESISTANCE OF 3% OPEN PLATE PLUS 36% OPEN BRASS SCREEN

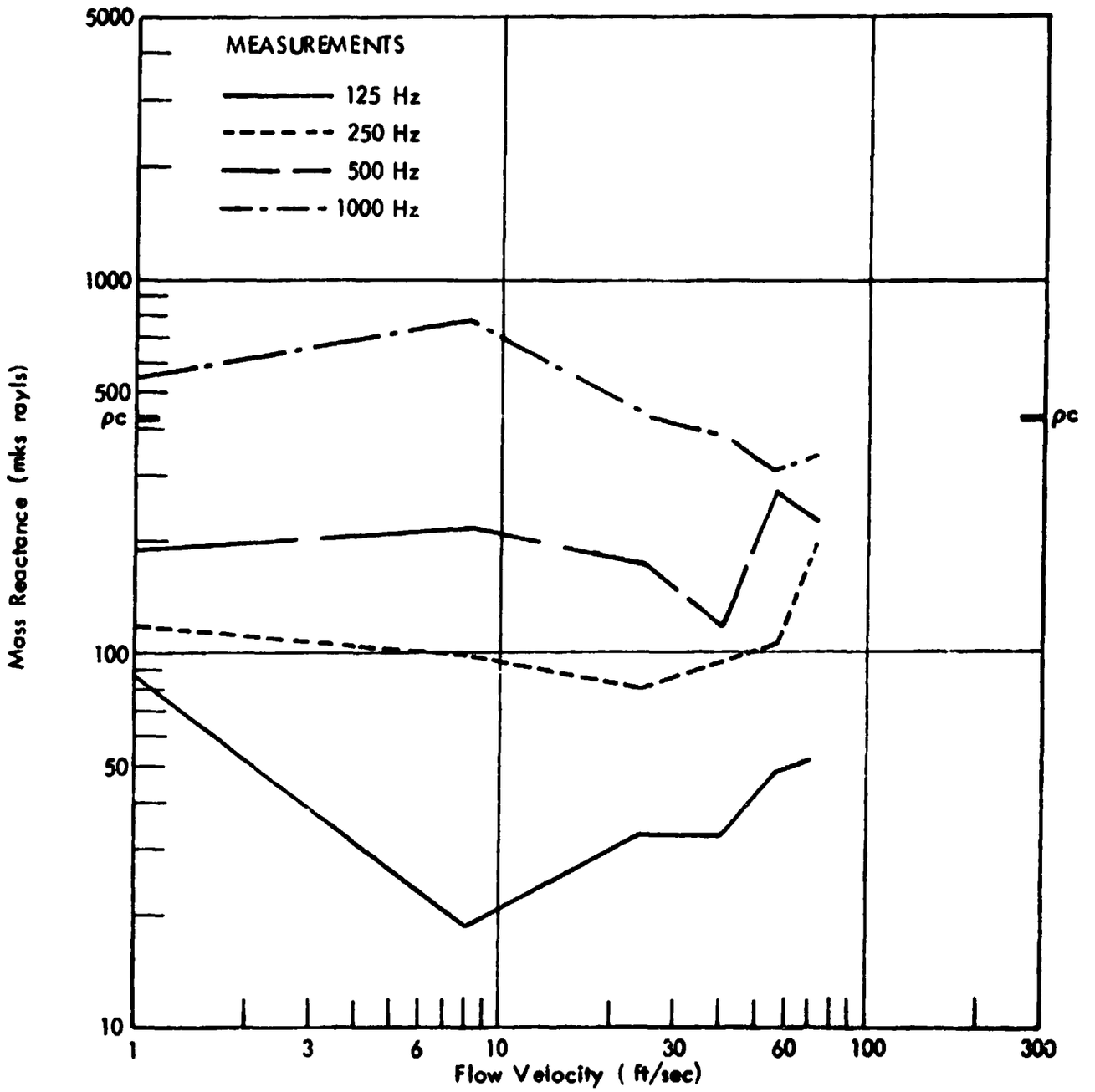

FIGURE 25. REACTANCE OF 3% OPEN PLATE PLUS 36% OPEN BRASS SCREEN

3.0 MUFFLER CONFIGURATION EFFECTS

The acoustic performance of the 80 x 120 foot wind tunnel muffler will depend not only on the acoustic impedance of the muffler liner, but to a large extent on configuration details and wind effects. In order to explore various configuration effects and obtain design data for a variety of full-scale configurations, NASA Ames Research Center personnel have conducted an extensive series of tests in the 7 x 10 foot wind tunnel.

These tests have provided invaluable data for the baseline fiberglass and perforated plate configurations, have provided insight into various modifications of these baseline designs, and have served to uncover various potential performance problems. In this section the baseline configuration performances determined from the wind tunnel tests are compared with the design goal, and the deficiencies quantified for various operating conditions. Configuration changes of three types for providing additional acoustic attenuation to alleviate the predicted discrepancies and to provide additional conservatism in the design are then described.

3.1 Baseline Designs and Performance

Figure 26(a) is a plan view of the three full-scale baffles mounted in the 7 x 10 foot wind tunnel at NASA Ames Research Center. The streamlined two-way noise source with broadband capability can be mounted alternately upstream of the muffler for exhaust muffler testing or downstream of the muffler for inlet testing. The four microphones traversing the center duct in Fig. 26(a) are used to determine muffler performance per unit length. The baseline fiberglass configuration shown in

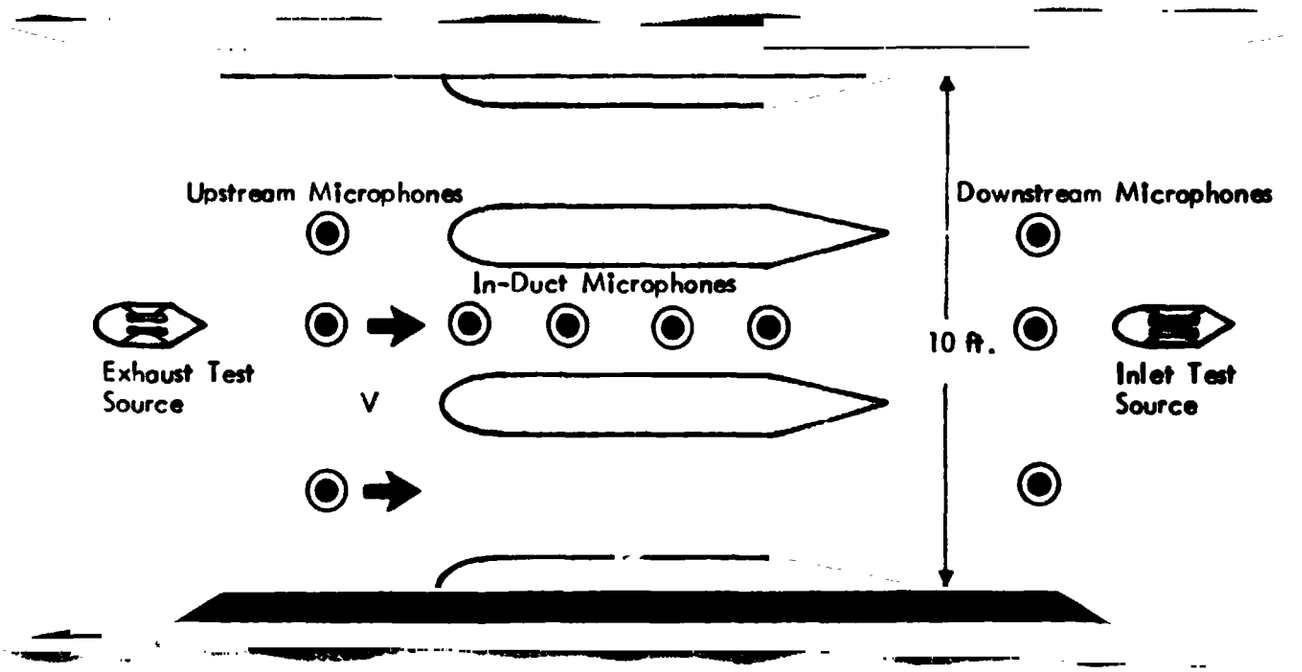

(a) Plan View of 7 x 10 ft. Wind Tunnel NASA Ames 3 Baffle Full Scale Test Rig

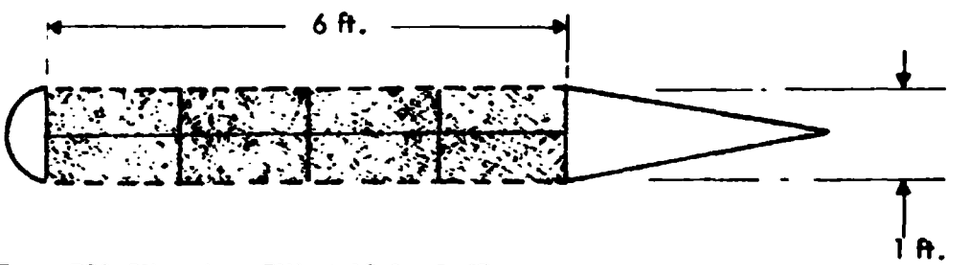

(b) Baseline Type 701 Fiberglas Filled 10 ft. Baffle

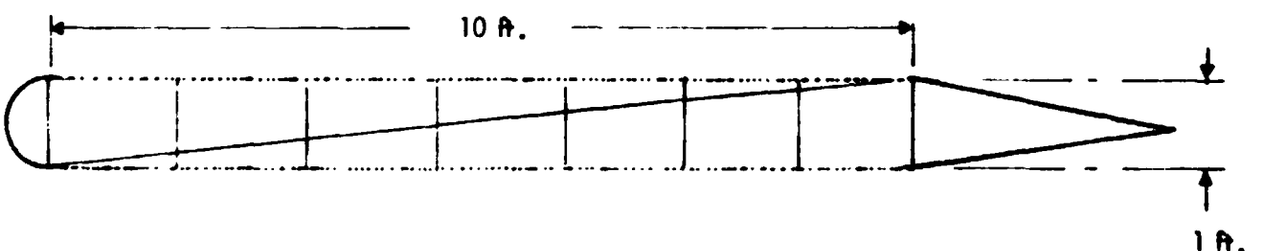

(c) Baseline 3% Open Perforated Plate 14 ft. Baffle

FIGURE 26. NASA AMES 7 x 10 FT. WIND TUNNEL TEST CONFIGURATION AND BASELINE DESIGNS

Fig. 26(b) utilizes a 6-foot section of Type 701 Fiberglas partioned with a lengthwise center impervious plate and with three equally spaced transverse plates. The fiberglass was covered with a 33% open perforated plate.

The baseline 3% open perforated plate configuration is shown in Fig. 26(c). The test results reported were generated with a baffle containing a 6-foot long absorbing section, and those results were extrapolated to the 10-foot long section shown in Fig. 26(c), using the induct microphone data. In the perforated plate muffler tests, the 6-foot section was again segmented by three equally spaced transverse partitions, but the lengthwise partition slanted from one side of the baffle at the leading edge to the opposite side at the trailing edge of the treated section. Preliminary cost analyses by NASA Ames personnel indicate that the 10-foot long perforated plate section muffler will cost approximately the same as the baseline fiberglass-filled muffler with 6 feet of acoustic treatment.

The results of the wind tunnel tests and analyses conducted by NASA Ames Research Center personnel on the acoustic performance of these two baseline muffler configurations for the inlet and exhaust cases are shown in Figs. 27 and 28, respectively. If the zero and maximum velocity inlet and exhaust configuration muffler performances presented in Figs. 27 and 28 are taken in aggregate, the fiberglass and perforated plate configurations have comparable performance. In general, the performance of the fiberglass design can be improved by lengthing the treated test section. An exception to this is the inlet muffler configuration in the high frequency regime where the sound beams down the center of the channels limiting the insertion loss to approximately 10 dB.

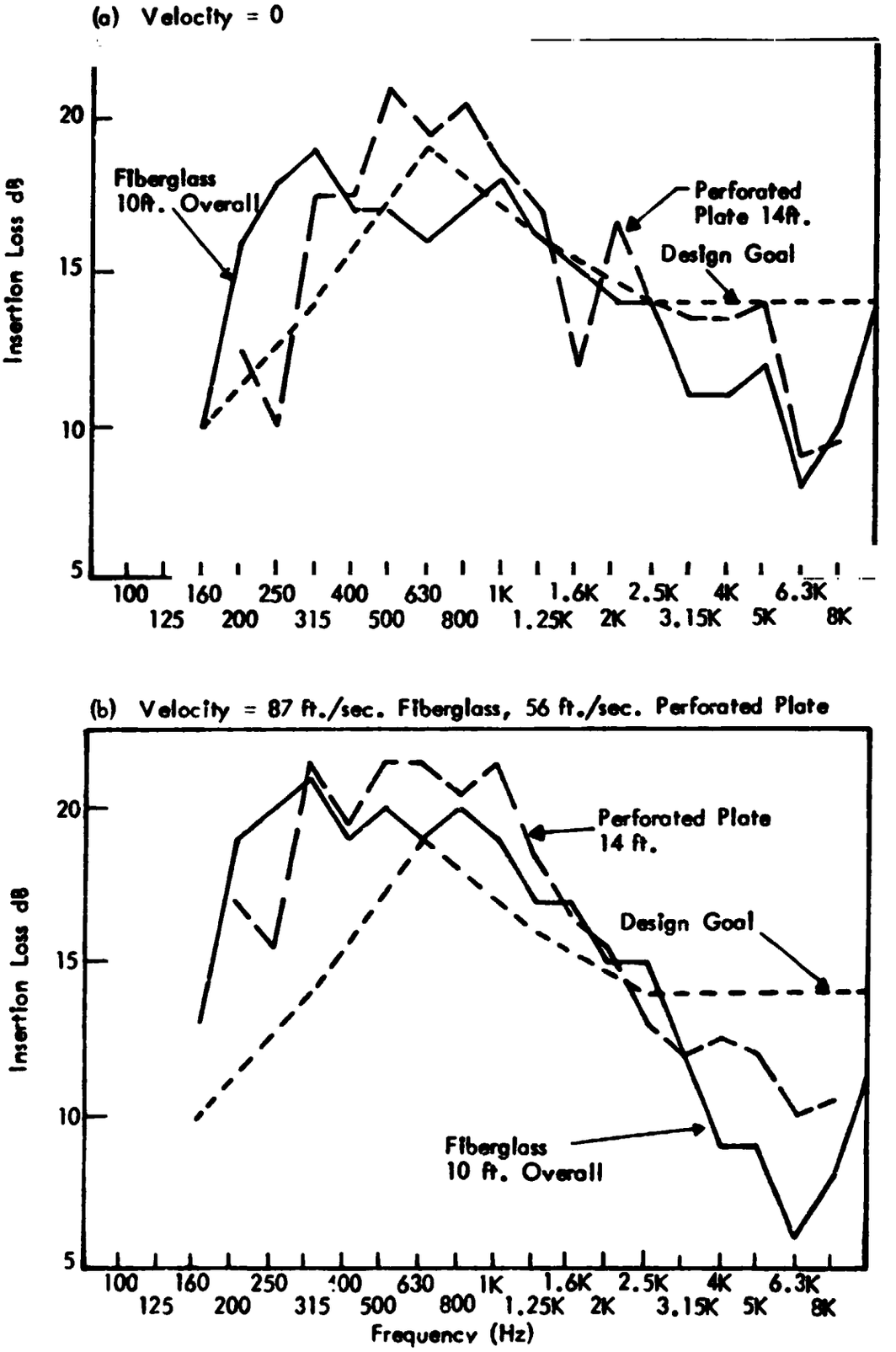

FIGURE 27. INLET MUFFLER PERFORMANCE PREDICTED FROM NASA AMES 7 x 10 FT. WIND TUNNEL TESTS (Perforated Plate Data Extrapolated From 10 ft. to 14 ft.)

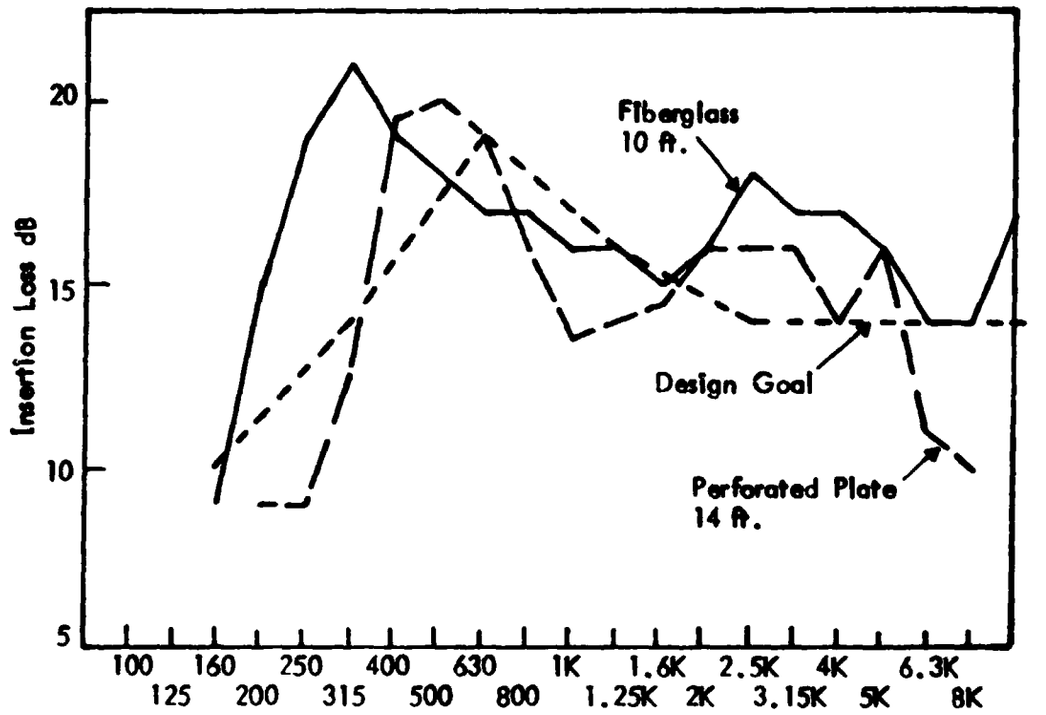

(a) Velocity = 0

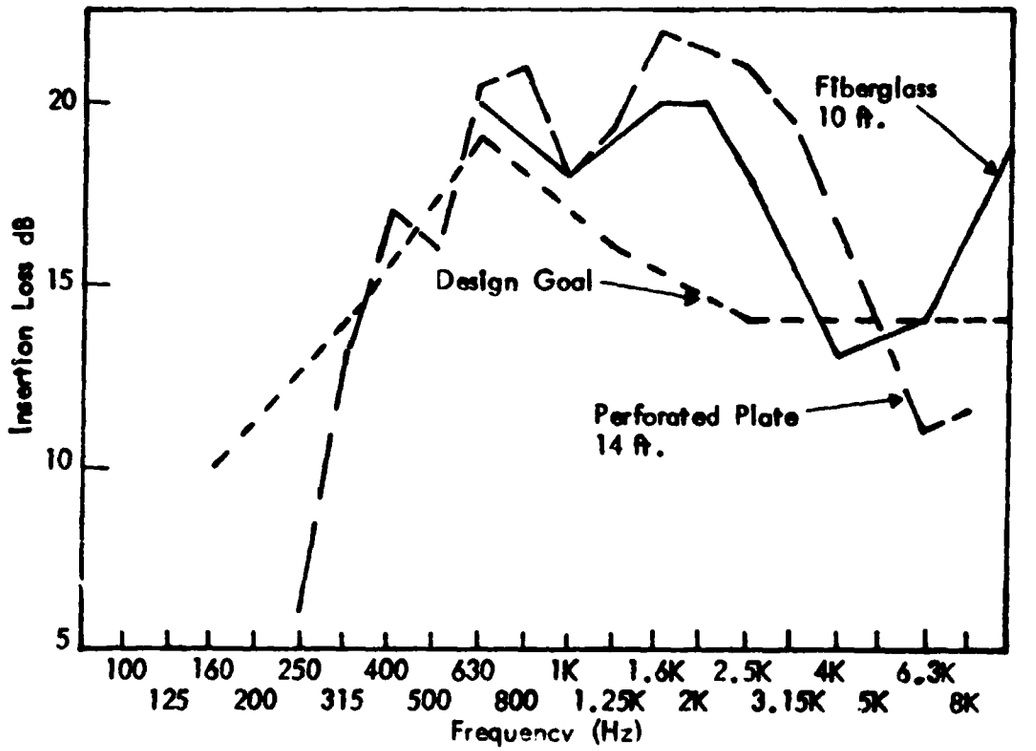

(b) Velocity = 120 ft./sec.

FIGURE 28. EXHAUST MUFFLER PERFORMANCE PREDICTED FROM NASA AMES 7 x 10 FT. WIND TUNNEL TESTS (Perforated Plate Data Extrapolated From 10 ft. to 14ft.)

In addition to further increasing the length of the perforated plate design, a number of other acoustic performance enhancement techniques are available and will be described in subsequent parts of this section. For reference, the deficiencies between the 14-foot perforated plate muffler performance and the design goals are tabulated from Figs. 27 and 28 in Table 4. In general terms, there is a 2 to 3 dB average deficiency at frequencies below 200 Hz and above 2,000 Hz.

TABLE 4
DESIGN DEFICIENCIES OF 14 FT. PERFORATED PLATE MUFFLER (dB)

	125	160	200	250	315	400	500	630	800	1000	1250	1600	2000	2500	3150	4000	5000	6300	9000
INLET																			
v = 0			3								3			1	1		5	4	
v = 56 ft/sec		2	4										2	3	2	2	4	3	
EXHAUST																			
v = 0		2	3	1				1	2	2							3	3	
v = 120 ft/sec			6	1		1											3	2	

3.2 Curved Baffles

From an acoustics point of view, curving the baffles to block the line of sight is the most powerful technique for obtaining greater performance than the baseline design configurations, which are already highly optimized. A suggested curved baffle configuration designed to block the line of sight and minimize effects on flow is shown in Fig. 29(a). This design is achieved

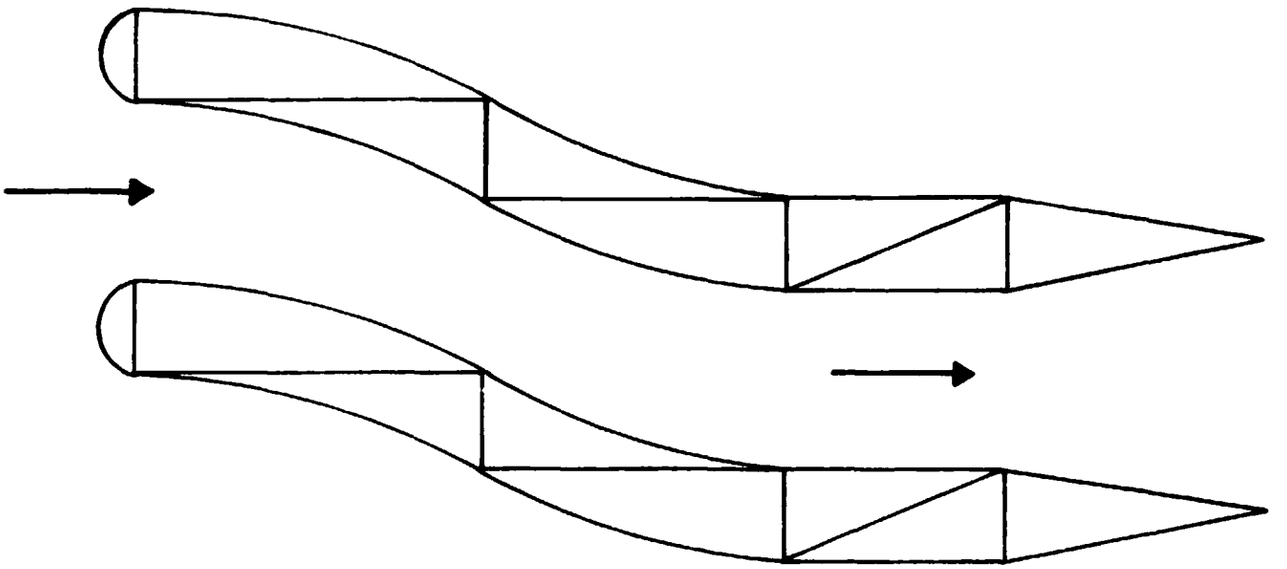

(a) Line-of-Sight Blocked Configuration

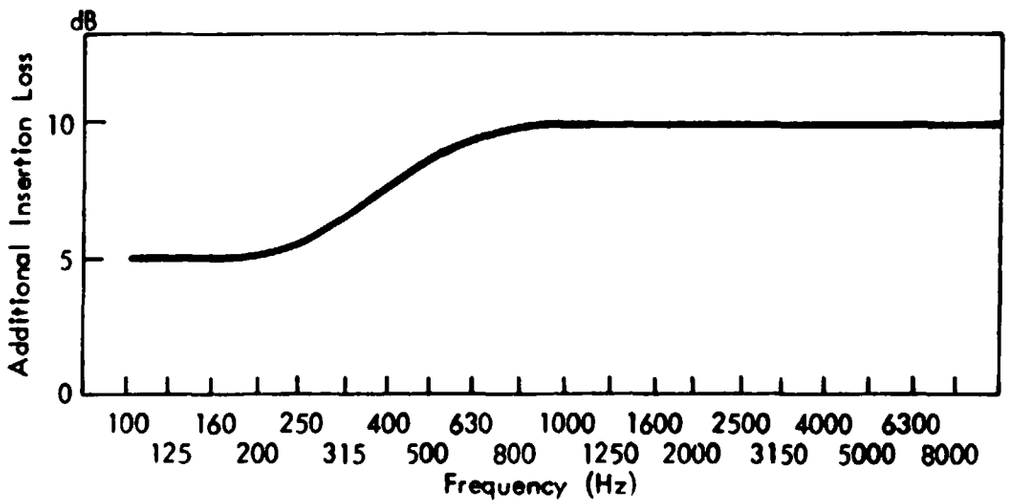

(b) Additional Loss Relative to Straight Configuration

FIGURE 29. HIGH ACOUSTIC PERFORMANCE LINE - OF - SIGHT BLOCKED CONFIGURATION

by translating the tail section of each baffle 2 feet to the side and connecting the nose and tail with a 7-foot S-shaped perforated section followed by a 3-foot straight perforated section before the tail. The additional acoustic attenuation provided by the curved baffles relative to the straight baffle configuration is estimated in Fig. 29(b). This estimate, which is 5 dB of additional loss in the low frequency regime and 10 dB additional loss in the high frequency regime, was scaled from measured data for the Sound-Stream muffler configuration described in Reference 11. NASA Ames personnel are in a better position than the authors to determine the feasibility of such a curved baffle design for use as the inlet or exhaust muffler and to generate alternate curved designs and estimates of the effect on wind tunnel flow conditions.

3.3 Partition Design

A number of variations of the length-wise and transverse silencer partitions have been investigated by BBN and NASA Ames with a view toward optimizing muffler performance. For example, the diagonal lengthwise partition of the type shown in Fig. 26(c) was used in the NASA Ames wind tunnel test in order to eliminate whistles caused by cavity resonances (see next section).

The performance of a perforated plate muffler configuration with no fuzz is generally enhanced at frequencies associated with half-wave resonances between the transverse partitions. Thus the performance of the baseline design with approximately 20-inch partition separation is quite good in the vicinity of 350 Hz. Changing the transverse partition spacing from

20 inches to 40 inches in the 10-foot length section should further enhance the muffler performance in the lower frequency regime.

Previous work, in particular the Reference 12 patent, shows enhanced duct liner attenuation when the depth of the liner is varied in steps along the muffler length. In order to investigate applicability of this concept the 80 x 120 foot wind tunnel muffler, a number of tests were conducted at BBN using a fiberglass-lined configuration. Results are shown in Fig. 30. Four configurations were tested: A baseline center partition, a ramp such as was used in the NASA Ames test with the 3% perforated plate configuration, a sawtooth configuration, and a sawtooth with a 0.3% perforated partition.

The ramp and sawtooth configurations gave poorer performance than the baseline; but the perforated sawtooth gave improved performance, particularly in the low frequency regime from 160 to 250 Hz. Because of the difference in absorption mechanisms in the fiberglass and perforated plate designs, these types of tests need to be repeated for a perforated plate muffler exposed to grazing flow. It might be inferred from the BBN tests that the ramp used to control whistles in the NASA Ames perforated plate muffler slightly degraded performance over that would be obtained with a non-whistling center partition in the frequency range from 250 to 500 Hz.

The increased performance of the perforated partition design in Fig. 30 also might merit additional investigation for the perforated plate muffler. The motivation for using a slightly perforated partition is to provide enough reactance so that the two sides of the muffler are essentially acoustically independent, and the high acoustic velocities are still obtained

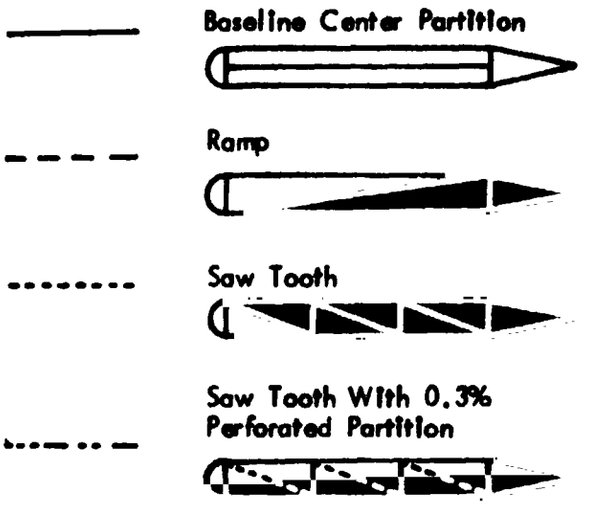

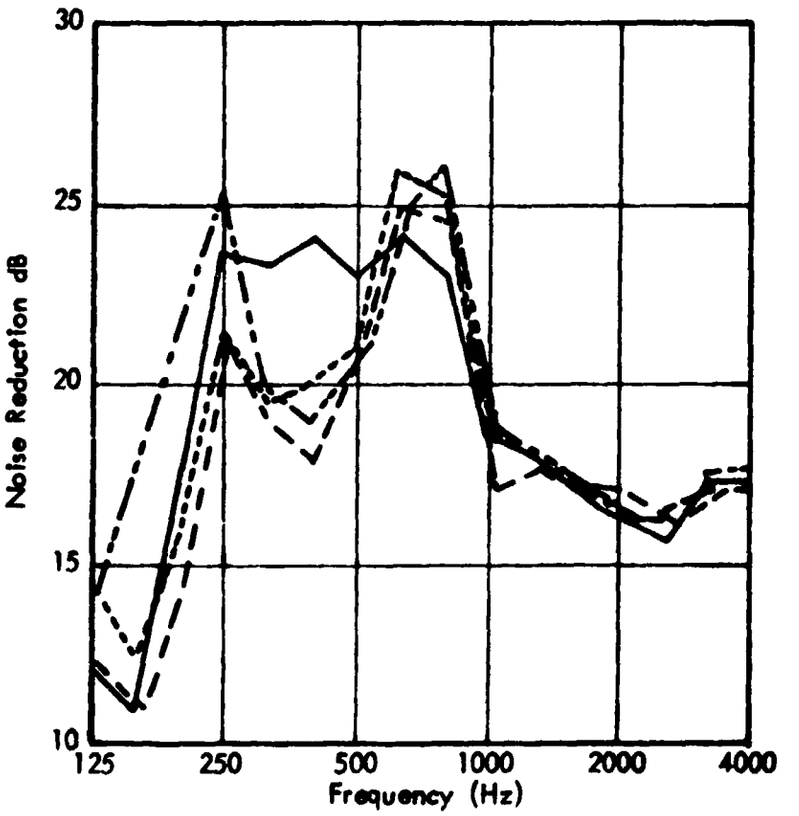

FIGURE 30. PERFORMANCE OF VARIOUS STAGGERED PARTITIONS IN BBN FIBERGLASS TESTS

at the muffler face for the 500 Hz design frequency. However, the slight perforation provides some flow resistance and therefore additional loss at the partition where the pressure gradients are very high.

The performance characteristics for a 1% open perforate with zero flow can be taken from Figs. 22 and 23. The figures show that the mass reactance varies from approximately 300 to 1500 mks rayls for frequencies between 250 and 1000 Hz, and the resistance varies from approximately 100 to 250 mks rayls over the same frequency range. In view of the measured factor of three increase in impedance when the percentage open area was changed from 3% to 1%, one might expect these values to increase by another factor of three for 0.3% open plate. Tests might be conducted with both 1% and 0.3% perforated partitions to determine the optimum.

3.4 Whistles and Wind Noise

Early tests conducted with the 3% perforated plate muffler configuration with a central lengthwide partition were plagued with very loud grazing-flow-generated whistles. This phenomenon was investigated analytically and experimentally in Reference 13. The frequency of the whistles in the NASA Ames tests correlated very closely with the grazing-flow velocity and hole diameter when a Strouhal number of 0.2 was used. When the flow velocity was increased, either by increasing tunnel speed or by blocking part of the channels, the whistle frequencies in the NASA Ames tests would jump progressively through those frequencies characteristic of half-wave resonances in the cavity depth.

Figure 31(a) illustrates a number of candidate techniques

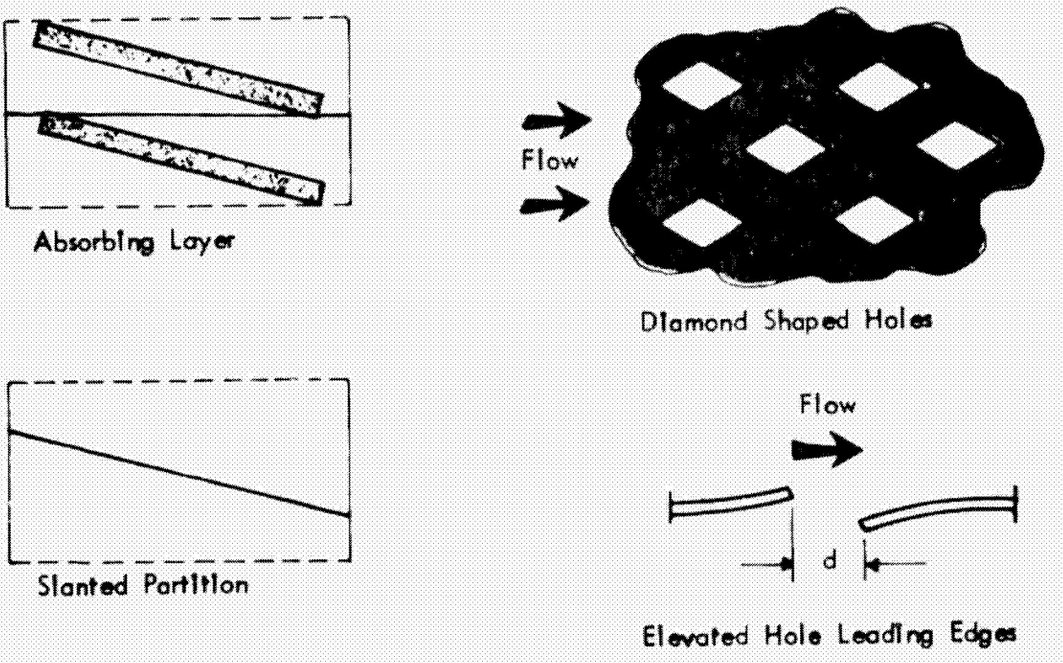

(a) TECHNIQUES FOR WHISTLE ELIMINATION

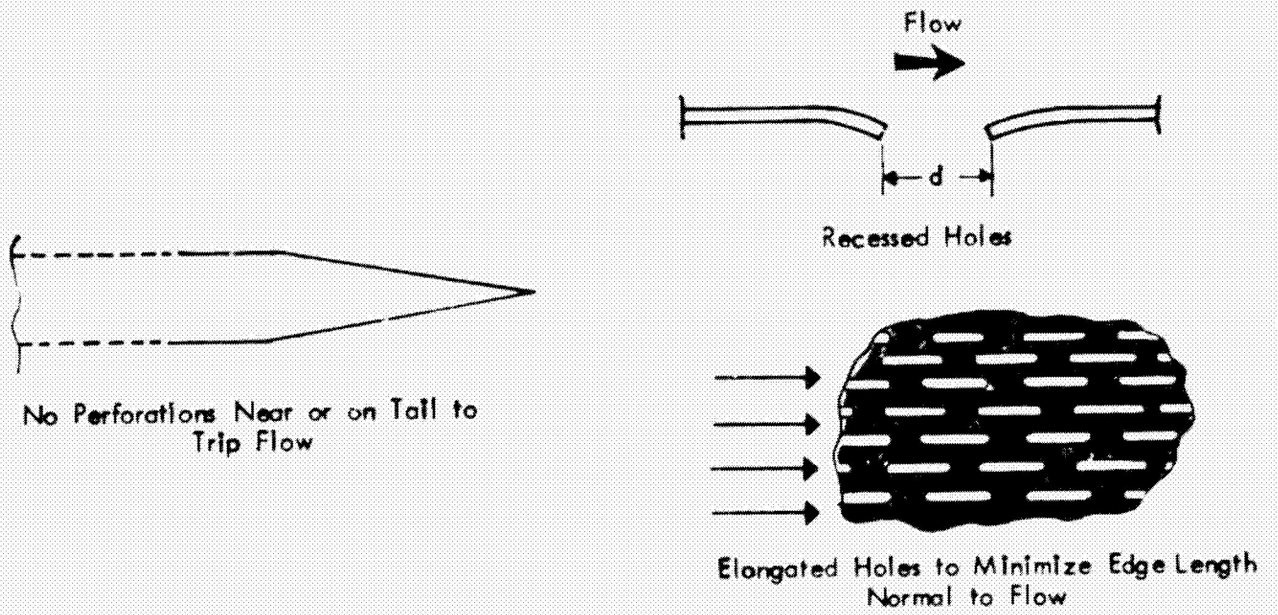

(b) TECHNIQUES FOR MINIMIZING WIND NOISE

FIGURE 31. CANDIDATE PERFORATED PLATE DESIGNS FOR MINIMIZING MUFFLER SELF-NOISE

for eliminating whistles in a perforated plate muffler configuration. The techniques illustrated on the left hand side of Fig. 31(a), namely, using a thin absorbing layer in the cavities and slanting the center partition, were used effectively in subsequent NASA Ames tests with the 3% open muffler configuration. The techniques on the right-hand side of Fig. 31(a) are suggested on the basis of previous BBN experience. By making the perforation holes diamond-shaped rather than circular, the singular hole diameter dimension which determines the frequency of the whistle is eliminated. The second concept involves punching the perforated holes so as to elevate the hole leading edges and depress the trailing edges so that the free shear layer does not oscillate at the hole trailing edge.

NASA Ames wind-tunnel tests of the 3% open perforated plate muffler with grazing flow velocities of 120 feet/sec indicated that the perforated plates generated wind noise which limits the noise reduction provided by the muffler in the high frequency regime around 4000 Hz. Although no technique will eliminate self noise generated by perforated plates exposed to grazing flow, several candidate techniques are available for minimizing this self noise. The muffler configurations tested in the 7 x 10 foot wind tunnel utilized a perforated tail section for possible enhanced acoustic performance. This may have contributed to flow instability just downstream of the start of the diffuser tail section. If this mechanism proves important for self noise generation, it might be eased by eliminating the perforations on the tail and even for a short distance upstream as illustrated on the left in Fig. 31(b).

A second candidate technique for minimizing wind noise would be to manufacture the perforated plates so that the hole lips are slightly indented into the plate thus removing the edges somewhat from the shear layer. A third candidate technique for minimizing flow noise due to the grazing flow is to elongate the holes along the direction of flow so that the hole edge length perpendicular to the flow velocity is small. These latter two techniques must be viewed as speculative and subject to experimental verification, because the flow pattern in the vicinity of the hole involves a complicated interaction of the grazing and acoustic flow velocities as described in Reference 7.

REFERENCES

1. J. S. Bendat and A. G. Piersol, *Random Data: Analysis and Measurement Procedures* (J. Wiley & Sons, N.Y., 1971), p. 314.

2. Bruel & Kjaer, "Standing Wave Apparatus Type 402 Instructions and Applications," Copenhagen, Fig. 6 or 7.

3. K. A. Hollin and M. H. Jones, "The Measurement of Sound Absorption Coefficient in Situ by a Correlation Technique," *Acustica*, Vol. 37 (1977).

4. U. Ingard and P. Morse, *Theoretical Acoustics* (McGraw-Hill, N.Y., 197_), p. 468 - 474.

5. Reference 4 p. 385 and 472.

6. U. Ingard and H. Ising, "Acoustic Nonlinearity of an Orifice," *J. Acoust. Soc. Am.*, Vol. 42, No. 1, 1967, p. 6-17, Eqs. 11 and 12.

7. T. Rogers and A. S. Hersh, "The Effect of Grazing Flow on the Steady State Resistance of Square-Edged Orifices," AIAA paper 75-493, Hampton, Va., March 74-26, 1975, Eqs. 33, 35, and 36(a).

8. U. Ingard, "On the Theory and Design of Acoustic Resonators," *J. Acoust. Soc. Am.*, Vol. 25, No. 6, 1953.

9. Ref. 6., Eq. 14 and ensuing discussion.

10. L. Beranek, *Noise and Vibration Control*, McGraw-Hill, N.Y., 1971, p. 503.

11. Reference 10. pp. 382-384

12. W. Zoramski, *Noise Suppressor*, U.S. Patent 3,830,335, May 14, 1973.

13. C. Y. Tsui and G. A. Flandro, "Self-induced sound generation by flow over perforated duct liners," *J. Sound Vib.*, **50**, 3, 315-332, February 1977